Stability and Adaptability in Balance:
A Dual Mechanism for Metaplasticity in Cortical Networks

Tea Tompos[1*], Fleur Zeldenrust[1] and Tansu Celikel[2*]

[1]Donders Institute for Brain, Cognition and Behaviour, Radboud University, Nijmegen, Netherlands

[2]Georgia Institute of Technology, Atlanta, GA, USA

*Correspondence should be addressed to Tea Tompos (t.tompos@neurophysiology.nl) and Tansu Celikel (celikel@gatech.edu)

1. Abstract

Metaplasticity dynamically adjusts how synaptic efficacy and connectivity change, helping neural circuits adapt to experience. However, the interaction between changes in synaptic weight (W) and connection probability (P) remains poorly understood. We explored their interaction using a biologically-inspired, multi-layer spiking neural network. We found that while W controls network excitability, P exerts layer-specific and time-dependent control, crucial for network stability. Simultaneous changes in W and P, i.e. metaplasticity, revealed complex, non-additive interactions, shaping response timing and neural recruitment, resulting in the emergence of functionally distinct neuronal subtypes: input-invariant neurons maintaining responsiveness and variant neurons enabling adaptation, based on differential E-I dynamics. This interaction allows the network to achieve functional homeostasis in the input layer while preserving flexibility in superficial layers. We provide a novel framework for understanding how metaplasticity balances the competing demands of stability and adaptability in cortical circuits, with significant implications for learning, memory, and neural coding.

2. Introduction

Neural circuits exhibit remarkable adaptability, constantly reshaping their connectivity and function in response to experience[1,2]. This adaptability relies not only on synaptic plasticity – the ability of individual synapses to strengthen or weaken – but also on metaplasticity, a higher-order mechanism that governs how plasticity itself changes over time[3,4]. We define metaplasticity formally as the modulation of subsequent synaptic plasticity expression by prior plasticity events. This "plasticity of plasticity" ensures that neural circuits remain responsive to new information without succumbing to runaway excitation or complete silence, enabling both learning and the maintenance of stable representations[5,6].

The expression of synaptic plasticity, and thus metaplasticity, hinges on the interplay of at least two fundamental, yet often independently considered, synaptic parameters: synaptic weight (W) and connection probability (P). Synaptic weight, reflecting the strength of individual synaptic connections, determines the magnitude of postsynaptic responses to presynaptic activity [1,7–9]. Connection probability, conversely, reflects the likelihood that two neurons are functionally connected, shaping the overall architecture and information flow within a network [10–12]. Prior neuronal activity can modulate synaptic weights by shifting the thresholds for inducing LTP or LTD [2,13–16], altering the direction and magnitude of subsequent synaptic changes [17]. For instance, prior NMDA receptor activation can elevate the LTP induction threshold, requiring stronger stimuli to elicit potentiation, while weaker stimuli might favor LTD [17]. Although NMDA receptor activation is necessary to initiate synaptic plasticity, it subsequently suppresses plasticity induction *in vitro* and *in vivo,* whereas mGluR activation contributes to further expression of plasticity [17]. This activity-dependent adjustment allows for a dynamic, context-sensitive control over synaptic modification, balancing the competing forces of potentiation and depression.

Prior activity can also alter the magnitude and persistence of synaptic changes through mechanisms such as the upregulation of protein synthesis, modifications in ion channel function, or changes in intrinsic cellular excitability[17,19–21]. Critically, these changes can also impact the probability of forming or eliminating synaptic connections, thereby directly modulating P [12]. These simultaneous, interdependent changes in W and P introduce coupled yet functionally distinct layers of regulation, allowing neural networks to adapt to activity-dependent signals dynamically. This constitutes the structural basis of metaplasticity.

The coupling of the changes in synaptic strength and connectivity discussed above is essential for maintaining homeostasis in neural systems, enabling synapses to adjust to

environmental demands without compromising network stability. Although synaptic mechanisms that contribute to metaplastic regulation by modifying both synaptic strength and the likelihood of forming new connections are well established[7,15,19,22], how this bi-directional relationship affects the functional organization of the neural circuits remains unknown. To answer this question, in this study, we developed a reduced, biologically inspired multi-layer spiking neural network model inspired by the rodent primary somatosensory cortex (S1). The conductance-based model integrates anatomical and physiological constraints drawn from empirical data. To emulate metaplasticity, we systematically scaled W and P relative to baseline values over a symmetric two-dimensional parameter space, thereby mimicking the processes of synaptic potentiation/depression and pruning/growth.

Our results demonstrate that metaplasticity operates through a dual mechanism: W primarily governs network activity, whereas P exerts layer-specific and context-dependent control. Weight and connection probability interact non-linearly, reshaping neuronal response amplitude, timing, and input selectivity. This relationship drives the emergence of functionally distinct neuronal subtypes – input-invariant neurons maintaining responsiveness and variant neurons enabling adaptation – based on differential E-I balance dynamics controlled by recurrent and feedforward inputs. *This interaction allows the network to achieve functional homeostasis starting from the input layer while preserving flexibility in superficial layers.* This work provides a novel framework for understanding how metaplasticity, through the integrated control of synaptic strength and network connectivity, balances the competing demands of stability and adaptability in cortical circuits, with significant implications for learning, memory, and neural coding.

3. Results

To investigate how metaplasticity regulates network dynamics, we quantified population-specific activity changes in a biologically inspired, reduced spiking neural network model of the canonical layer (L) 4→L3/L2 microcircuit, consisting of Hodgkin Huxley neurons (Figure 1a, Online Methods). The network incorporated layer-specific differences in connectivity and neuron types (Figure 1b, Online Methods, and Supplementary Figure 1) based on anatomical and physiological data [10,23–29]. We specifically aimed to determine the interaction between synaptic weight (W) and connection probability (P) while expressing metaplasticity in the network. Metaplasticity was emulated by systematically scaling W and P across a two-dimensional parameter space (Figure 1c), mimicking the effects of synaptic potentiation (W>1), synaptic depression (W<1), synapse addition (P>1), synaptic elimination (P<1) and any combination thereof (Figure 1d,e).

3.1 Synaptic Weight Dominates Connectivity Probability in Gating Population Activity

We quantified population activity in cortical network layers as the total number of spikes in response to discrete inputs (i.e., thalamic population spiking; Supplementary Figure 1c, Online Methods). Varying W and P revealed asymmetric changes in network activity (Figure 2a, Supplementary Figure 2a,b), suggesting differential roles for W and P within metaplasticity. Notably, changes along the synaptic weight axis had a much greater impact on spike output than changes along the connection probability axis. Increasing W consistently increased spiking activity across all populations, whereas decreasing W suppressed activity (Figure 2a). Increasing P, moreover, could not rescue the activity of networks with depressed synaptic weights (Figure 2a, lower right quadrant). These results establish synaptic weight as the primary driver of network activity during metaplasticity.

3.2 Connectivity Probability Modulates Activity in a Layer-Specific Manner

While W dominated the overall activity, P exerted a more nuanced, layer-specific influence, which depended on W. To dissect these effects, we compared the activity changes along specific “plasticity pathways” (Figure 2b: isolated changes in W, solid red line; isolated changes in P, solid blue line) to “metaplasticity pathways” (i.e. changes in W after doubling P, dashed red line; changes in P after doubling W, dashed blue line).

Doubling weights without changing connection probabilities (Figure 2c: solid red line) increased spike output in all layers, but the magnitude of the increase was layer-dependent (L4:

moderate, slopes > 0; L3/L2: strong, slopes >> 0; Figure 2c, see slope values next to panels). In contrast, doubling P without changing W (Figure 2c: solid blue line) exerted negligible effects (slopes ≈ 0).

Within a metaplastic context, when the network was “primed” by first scaling one parameter, subsequent changes in the other parameter produced layer-specific effects. Potentiation after growth (Figure 2c: dashed red line) generally increased the activity, similar to the impact of increasing W alone. However, growth after potentiation (Figure 2c: dashed blue line) led to bidirectional changes, with activity suppression in L4 and L2I (Figure 2c, slopes < 0), and amplification in L3 and L2E (slopes > 0). These results indicate (1) the existence of the order effect within metaplasticity pathways: potentiation followed by growth yields weaker effects than growth followed by potentiation, and (2) that, while W is the dominant factor controlling overall network activity, P exerts metaplasticity-dependent, layer-specific modulatory influence on activity, particularly in the superficial layers.

3.3. Metaplasticity Promotes Non-Linear Interactions between W and P

After assessing their (in)dependent effects, we investigated how W and P interact in time. The combined impact of scaling W and P (W2P2) was not a linear sum of the individual effects (W2P1 and W1P2). To quantify this interaction, we examined the temporal dynamics of spiking in four key network states: baseline (W1P1), potentiation (W2P1), growth (W1P2), and potentiation with growth (W2P2) (Figure 2d, Supplementary Table 6).

In the baseline network (W1P1, Figure 2e, black), each layer exhibited distinct temporal response profiles. L4 neurons showed an immediate peak in activity following stimulus onset, followed by a rapid decay. Superficial layers (L3/L2) showed progressively sparser and lower-amplitude responses, in line with empirical observations from the same network measured *in vivo*[30–32]. Potentiation (Figure 2e: blue) increased the spike rates (vertical shift) and prolonged the activity duration (horizontal spread) across all populations, revealing the origins of the increased activity observed in Figure 2a,c. Synaptic growth (Figure 2e: orange) had minimal effects on firing in all populations. In the metaplastic W2P2 state (Figure 2e: pink), however, L4 firing rates were reduced compared to the W2P1 state, falling below the level imposed by potentiation alone. In contrast, superficial layers maintained a high activity level. This suggests a layer-specific "ceiling effect" imposed by W, with metaplasticity operating below (in L4) or near this ceiling (in L3/L2).

To quantify the temporal interaction between W and P, we calculated the ratio of activity in the W2P2 state to the sum of activities in the W2P1 and W1P2 states (Figure 2f, Online

Methods). In L4, this interaction was sublinear throughout the stimulus presentation window (Figure 2f, bottom), indicating that W and P in combination exert a lower impact on the activity than summing their individual effects would suggest. In contrast, superficial layers exhibited a temporal switch in W-P interaction dynamics: sublinear in the first half of the stimulus window (0-30 ms) and supralinear in the second half (30-60 ms) (Figure 2f, middle and top). This temporal switch occurred earlier in L3 (I neurons at 28.5 ms, E neurons at 31.5 ms) than in L2 (I neurons at 34.5 ms, E neurons at 37.5 ms). These results demonstrate a complex, non-linear, bimodal, and time-dependent interaction between W and P.

3.4. Active Neurons Show Layer-Specific Recruitment Rates And Activity Modulation Under Metaplasticity

To dissect the mechanisms underlying the metaplasticity-driven changes in population spiking, we investigated two potential contributing factors: (1) changes in the fraction of active neurons (i.e., the active pool size) and (2) changes in the firing frequencies of already active neurons.

We first examined how W and P scaling affected the recruitment of neurons into the active pool in each population (Figure 3a, Supplementary Table 7). Consistent with the activity results of the previous sections, changes in active pool size were most pronounced in the superficial layers (L3 and L2). However, there was no direct correspondence between changes in activity (Figure 2a) and resizing in the active pool (Figure 3a), particularly in L4. For example, in L4E, synaptic potentiation and growth increased activity but decreased recruitment, thus shrinking the active neuron pool size, and driving increased spiking in remaining active neurons (Supplementary Figure 3a,b).

To isolate the effects of altered firing frequency in active neurons, we normalized the spiking activity in each time bin by the number of active neurons in that bin (Figure 3b, Online Methods). This analysis revealed that in L4, W strongly modulated the firing frequency of active neurons, both in the independent (W2P1, blue) and in the metaplastic condition (W2P2, pink). Doubling P alone (W1P2, orange) had only a minimal effect on the firing frequencies of active L4 neurons. In L3 and L2, W also modulated the active firing frequencies, but to a lesser extent than in L4. These findings indicate that changes in neuronal recruitment into the active pool and the firing frequencies of active neurons contribute to the overall changes in network activity, with their relative contributions varying across layers and conditions.

3.5. Connection Probability Stabilizes Input Selectivity Distributions

How does metaplasticity affect the input selectivity of individual neurons? We hypothesized that active pool resizing (Figure 3a) reflects shifts in the distribution of neuronal input selectivities. To test this, we calculated the fraction of inputs (i.e., discrete periods of thalamic activity, Supplementary Figure 1c; on average 32 different inputs per W-P condition) that elicited at least one spike from each neuron in the four key network states: W1P1, W1P2, W2P1, W2P2. Higher fractions indicate lower selectivities, rendering neurons easier to recruit and thereby expanding the active pool, and vice versa (Figure 4a,b).

In the baseline network (W1P1, Figure 4c, black), L4 neurons exhibited a broad distribution of input selectivities, with neurons responding to a wide range of inputs. L3 and L2 populations showed narrower ranges, that contained neurons with stronger input selectivities. Potentiation (W2P1, Figure 4c, blue) dramatically altered the selectivities in L4 ($p<0.001$; Kolmogorov-Smirnov test with Bonferroni correction), creating a bimodal distribution with a large proportion of neurons responding to very few and a small proportion to almost all inputs. In contrast, potentiation broadened the selectivity ranges of L3/L2 populations ($p<0.001$ in L2E; $p<0.005$, L3E, L2I; $p<0.01$ in L3I). These results explained the shrinkage of the active pool in L4 and its expansion in L3/L2 (Supplementary Table 7, Figure 3a), thus confirming the causal link between active pool resizing and neuronal selectivities.

In the metaplastic W2P2 state (Figure 4c, pink), the selectivity distributions were partially restored across all populations (W1P1 vs. W2P2: $p<0.001$ in L2E; $p<0.01$ in L3E, L2I; $p<0.05$ in L4I, L3I) compared to the W2P1 state. However, a greater proportion of neurons exhibited a high selectivity (responding to few inputs), especially in L4. Decreasing W (W1P2, Figure 4c, orange) fully restored the population-wide baseline selectivity distributions. While the W1P2 condition contains double the number of synapses compared to W1P1, overlaps between selectivity distributions in all layers suggest that P plays a crucial role in stabilizing these distributions, particularly in L4, counteracting the destabilizing effects of increasing W (W2P2 vs W2P1).

3.6. Metaplasticity Drives Emergence of Functionally Distinct Neuronal Subtypes through Regulation of Layer-Specific E-I Balance

To understand the basis for altered neuronal selectivities (Figure 4c), we classified neurons from four network states (W1P1, W1P2, W2P1, W2P2) based on their input responsiveness. Each neuron was assigned a binary code (1 if responded to ≥ 1 input, 0 if not) for each condition, resulting in three functional classes (Figure 5a): input-invariant neurons

(responded in all conditions), variant neurons (responded in some conditions but not others), and silent neurons (unresponsive in all conditions).

All cortical populations contained mixtures of input-invariant and variant neurons, while silent neurons emerged in the superficial layers (Figure 5b). This suggests a functional specialization universal for all populations, with input-invariant neurons ensuring baseline responsiveness and variant neurons contributing to network adaptability.

To identify causes driving the functional specialization into invariant and variant neurons, we analyzed the balance between excitatory and inhibitory presynaptic currents received by individual neurons (Figure 5c-f, Online Methods). First, we discovered that, at baseline (W1P1), less invariant neurons exhibited E-I balance (Figure 5g; black) compared to variant neurons (Figure 5h; black). Second, when comparing different conditions, variant neurons typically maintained a stable E-I balance across conditions (Figure 5h, Supplementary Figure 4b), whereas invariant neurons showed dynamic state shifts (Figure 5g, Supplementary Figure 4a).

Specifically, in L4, synaptic potentiation drove input-invariant neurons into E-dominated states (W1P1 vs W2P1, blue; $p<0.001$, Supplementary Figure 4a), while metaplasticity reversed this effect by shifting neurons into E-I balance (W1P1 vs W2P2, pink: $p<0.05$ in L4I, $p<0.005$ in L4E). Synaptic growth further promoted the reversal from E-states to balance (W1P1 vs W1P2, orange: $p<0.001$). In L3/L2, potentiation maintained invariant neurons in E-states but metaplasticity (W2P2) and subsequent W1P2 state facilitated their transition into E-I balance (W1P1 vs W2P2, pink: $p<0.001$ in L3E, $p<0.05$ in L2E; W1P1 vs W1P2, orange: $p<0.001$ in L3E, $p<0.05$ in L2E, L3I). According to these findings, W ensures the network's responsiveness by entirely disrupting the E-I balance in L4 while preserving original states in L3 and L2. In contrast, P has a strong restoratory role in all layers.

Both excitatory and inhibitory presynaptic currents were composed of mixed sources. To understand the origins of E-I balance, we dissected the presynaptic currents into recurrent (intralayer) and feedforward (interlayer) components (Supplementary Figure 5a, Online Methods). Significant differences in E-I states observed between invariant and variant classes in W1P1 (Figure 5g,h, black) were due to stronger recurrent inhibition (RCI) in variant neurons, along with weaker excitation carried via recurrent E (RCE) synapses in L4/L3 (Supplementary Figure 5b-d; $p<0.05$) and feedforward E synapses in L2 ($p<0.05$). Potentiation (W2P1; Supplementary Figure 5b-d) increased the gap in RCI and RCE currents between neuronal classes (W2P1), while metaplasticity (W2P2) and subsequent W1P2 state decreased it.

Extending the E-I balance analysis across the full two-dimensional (meta)plasticity space revealed distinct profiles for input-invariant and variant neurons. Variant neurons exhibited balance at lower W and P values (Figure 6b, white), indicating that balance emerged early and was consistently maintained across diverse W-P conditions, particularly under synaptic potentiation and growth (Figure 6b, top right quadrant). The early emergence of E-I balance in variant neurons happened sooner in L4 than L3/2, and sooner in E than I neurons. Conversely, invariant neurons frequently exhibited E-domination and less frequently achieved tight E-I balance, although the balance was observed under specific P-dependent conditions (Figure 6a, white).

A direct comparison of E and I currents highlighted that input-invariant neurons received markedly reduced inhibitory currents compared to variant neurons across most of the W-P landscape (Figure 6c, pink vs. blue lines; Supplementary Figure 6a,c), while differences in excitatory currents were less pronounced (Figure 6b, orange vs. black lines; Supplementary Figure 6a,b). This differential inhibitory drive is a key feature distinguishing the two functional subtypes.

4. Discussion

We investigated metaplasticity — the activity-driven interplay between synaptic weight (W) and connection probability (P), in a reduced, multi-layered spiking neural network with conductance-based neurons and synapses whose architecture was modeled after the rodent primary somatosensory cortex (S1). Our findings reveal a complex, non-linear interaction between these two fundamental mechanisms of plasticity, suggesting that metaplasticity orchestrates network dynamics through a dual mechanism: (1) a dominant modulation of activity primarily driven by synaptic weight changes and (2) a layer-specific and context-dependent regulation of network stability and response properties influenced by connection probability.

Our results demonstrate that synaptic weight is the primary determinant of overall network activity. Across all layers, increasing W consistently increased spiking output, while decreasing W suppressed it (Figures 2a,c). This finding aligns with the fundamental understanding of synaptic plasticity, where stronger synapses lead to a greater likelihood of a postsynaptic neuron firing [1,2,19,23,33]. The observation that even with an increased connection probability, the activity of a network with depressed synaptic weights (W<1) could not be rescued (Figure 2a, lower right quadrant) underscores the primacy of W in controlling the overall firing rate and the importance of Hebbian plasticity mechanisms, such as long-term potentiation (LTP) and long-term depression (LTD), in shaping the overall responsiveness of cortical circuits.

While W dominates the overall activity, P exerts a more nuanced, layer-dependent influence. In the input layer (L4), network activity remained remarkably resilient to changes in P, particularly when W was maintained at baseline levels (Figures 2a,c). This suggests that L4, the primary recipient of subcortical input, is configured for robust information relay, consistent with its role in sensory processing [24,34–36]. This robustness may be critical for maintaining stable representations of sensory stimuli, even amidst ongoing plasticity. In contrast, superficial layers (L3 and L2) exhibited a dramatic sensitivity to overall changes in both W and P. Even modest alterations could lead to substantial increases or complete suppression of activity (Figures 2a,c and 3a). This heightened sensitivity could be why L2 and L3 are the first layers to express experience-dependent plasticity, upon altered sensory experience[37]. The ability of P to bidirectionally modulate population activity in these layers (Figure 2c) highlights its role in fine-tuning network dynamics, possibly contributing to the emergence of complex computations and representations in higher cortical areas.

A key finding of our study is the non-linear interaction between W and P. The combined effect of scaling both parameters was unequal to the linear sum of their individual effects but rather a complex interaction that varied across layers and over time (Figure 2f). This non-linearity confirms the hallmark feature of metaplasticity — it is not a mere combination of independent plasticity mechanisms but a higher-order regulatory process that integrates changes in synaptic strength and connectivity in a dynamic and context-dependent manner.

The temporal analysis of spiking revealed that metaplasticity gates hierarchical interaction of W and P (Figure 2e). Specifically, we observed a time-dependent switch in W-P interaction dynamics in superficial layers, with sublinear interactions early in the stimulus window and supralinear interactions later (Figure 2f). This suggests that W dominates the initial response, setting the overall activity level. At the same time, P exerts a more prominent influence on later activity, potentially shaping the temporal evolution of the response and contributing to network stability. These temporal dynamics are critical because they suggest that metaplastic changes do not only influence if a neuron will spike but also when it spikes, potentially impacting the encoding of temporal information [38] and controlling further expression of plasticity through synapse-specific rules of spike-timing-dependent plasticity [9,10,33,39]. Metaplasticity differentially controlled neuronal recruitment dynamics across layers, adjusting the size of active pools of neurons (Figure 3a) and the firing frequency within the active population (Figure 3b) via changes in population-wide input selectivity distributions (Figure 4c). Pool resizing was most pronounced in superficial layers, suggesting that metaplasticity sculpts the size of the active neuronal ensemble in a layer-specific manner. This modulation of population sparseness (i.e., the fraction of active neurons) could optimize information coding and prevent runaway excitation [36,40,41].

Our analyses of four network states (W1P1, W2P1, W2P2, W1P2) provide snapshots of functional changes arising from structural crosstalk between synaptic weight and connection probability. We propose that these snapshots reflect a continuum of plasticity mechanisms, illustrating how networks navigate a dynamic landscape to balance adaptability and stability and achieve functional homeostasis (Figure 7). Along this continuum, networks exhibit dynamic functional states (W2P1, W2P2) that ultimately return to their baseline function (W1P1 ≈ W1P2), despite persistent metaplasticity-driven structural remodelling (W1P1 ≠ W1P2).

The W2P1 state, reflecting synaptic upscaling, is characterized by consistently elevated activity across layers. Mechanistically, L4 neurons increase their spiking by restricting the number of active neurons (Figure 3a), but active neurons ensure heightened responsiveness by lowering their input selectivities (Figure 4c) and transitioning from E-I balance to E-dominated

states (Figure 5g). L3/L2 achieve the same functional state by a different route: elevated spiking is mediated by recruiting more neurons (Figure 3a) with low input selectivities (Figure 4c) while maintaining their E-I balance (Figure 5g). We suspect that layer-specific mechanistic routes reflect the parallel forms of adaptability within the network upon connectivity changes.

The W2P2, embodying metaplasticity, combines the effects of upscaled W and P in a non-linear fashion to balance adaptability and subsequent stability. Notably, during the transition from W2P1 to W2P2, activity rates in L4 decline, whereas L3/L2 exhibit a persistent rise in activity. Despite significantly altered synaptic parameters, this downward trend in L4 suggests that metaplasticity, through coordinated adjustments in W and P, triggers a form of functional homeostasis. The mechanistic basis for the L4 activity decline involves a reduction in the active neuronal pool (Figure 3a), driven by heightened input selectivity (Figure 4c) and restoration of tight E-I balance from E-dominated states (Figure 5g).

The functional homeostasis continuum converges onto network stability through synaptic rescaling from W2P2 to W1P2. Throughout our results, we report the functional equivalence between W1P2 and W1P1, despite disparate underlying synaptic configurations. This underscores a fundamental principle: neural circuits can achieve similar functional outputs through diverse structural arrangements. This degeneracy, or "many-to-one mapping" between network structure and function [42,43], confers robustness and adaptability, allowing the network to navigate changing conditions while preserving essential computational capabilities. The layer-specific manifestation of this homeostatic effect – pronounced in L4, less so in L2/3 – reinforces the distinct functional roles of these cortical layers.

While the weight and connectivity changes in our model capture key aspects of metaplasticity, our approach has several limitations. First, the model is a reduced network, focusing on a simplified representation of S1: downscaled in size, with neurons as point integrators. Future work should incorporate more detailed anatomical and physiological features and their effects, including expanding neurons with dendritic compartments, implementing heterogeneity in neuronal subtypes, and more complex, structured connectivity patterns. The network changes do not presently differentiate between different plasticity rules at different synapses. Future extensions of this work will benefit from making W and P changes target specific synapses, depending on the identity of the pre- and postsynaptic neurons, and installing an active algorithm with interactive learning rules to capture dynamic connectivity changes in time. Second, our model focuses on feedforward processing, neglecting the role of feedback connections, which are crucial for cortical function. Therefore, the impact of P and W changes on feedback circuits is an important topic for future research. Finally, our analysis of

the pre-synaptic currents and how metaplasticity affects their balance (Figures 5 and 6) isolates inhibitory currents as a key driver of the observed shifts in E-I balance. This claim should be experimentally investigated to confirm the disproportional contribution of the inhibitory drive to neural network stability.

In conclusion, our findings demonstrate that metaplasticity, through the bidirectional, non-linear interaction between synaptic weight and connection probability, is a potent regulator of cortical circuit dynamics. By independently yet interdependently modulating these parameters, metaplasticity balances the need for stability (robustness in L4) and adaptability (flexibility in L2/3), enabling cortical circuits to maintain a reliable information processing capacity while adapting to changing environmental demands. This dual mechanism provides a framework for understanding how the brain learns and adapts while maintaining stable representations of the world.

References

1. Abbott, L. F. & Nelson, S. B. Synaptic plasticity: taming the beast. *Nat. Neurosci.* **3 Suppl**, 1178–1183 (2000).
2. Feldman, D. E. Synaptic mechanisms for plasticity in neocortex. *Annu. Rev. Neurosci.* **32**, 33–55 (2009).
3. Abraham, W. C. Metaplasticity: tuning synapses and networks for plasticity. *Nat. Rev. Neurosci.* **9**, 387 (2008).
4. Turrigiano, G. G. The self-tuning neuron: synaptic scaling of excitatory synapses. *Cell* **135**, 422–435 (2008).
5. Hulme, S. R., Jones, O. D. & Abraham, W. C. Emerging roles of metaplasticity in behaviour and disease. *Trends Neurosci.* **36**, 353–362 (2013).
6. Turrigiano, G. G. & Nelson, S. B. Homeostatic plasticity in the developing nervous system. *Nat. Rev. Neurosci.* **5**, 97–107 (2004).
7. Gallinaro, J. V., Scholl, B. & Clopath, C. Synaptic weights that correlate with presynaptic selectivity increase decoding performance. *PLOS Comput. Biol.* **19**, e1011362 (2023).
8. Allen, C. B., Celikel, T. & Feldman, D. E. Long-term depression induced by sensory deprivation during cortical map plasticity in vivo. *Nat. Neurosci.* **6**, 291–299 (2003).
9. Celikel, T., Szostak, V. A. & Feldman, D. E. Modulation of spike timing by sensory deprivation during induction of cortical map plasticity. *Nat. Neurosci.* **7**, 534–541 (2004).
10. Huang, C., Zeldenrust, F. & Celikel, T. Cortical Representation of Touch in Silico. *Neuroinformatics* **20**, 1013–1039 (2022).
11. Perin, R., Berger, T. K. & Markram, H. A synaptic organizing principle for cortical neuronal groups. *Proc. Natl. Acad. Sci. U. S. A.* **108**, 5419–5424 (2011).
12. Holtmaat, A. & Svoboda, K. Experience-dependent structural synaptic plasticity in the mammalian brain. *Nat. Rev. Neurosci.* **10**, 647–658 (2009).
13. Bear, M. F. Mechanism for a sliding synaptic modification threshold. *Neuron* **15**, 1–4 (1995).
14. Stanton, P. K. LTD, LTP, and the sliding threshold for long-term synaptic plasticity.

Hippocampus **6**, 35–42 (1996).

15. Lee, H.-K. & Kirkwood, A. Mechanisms of Homeostatic Synaptic Plasticity in vivo. *Front. Cell. Neurosci.* **13**, 520 (2019).
16. Bienenstock, E. L., Cooper, L. N. & Munro, P. W. Theory for the development of neuron selectivity: orientation specificity and binocular interaction in visual cortex. *J. Neurosci. Off. J. Soc. Neurosci.* **2**, 32–48 (1982).
17. Clem, R. L., Celikel, T. & Barth, A. L. Ongoing in vivo experience triggers synaptic metaplasticity in the neocortex. *Science* **319**, 101–104 (2008).
18. Huang, Y. Y., Colino, A., Selig, D. K. & Malenka, R. C. The influence of prior synaptic activity on the induction of long-term potentiation. *Science* **255**, 730–733 (1992).
19. Feldman, D. E. Synapses, scaling and homeostasis in vivo. *Nat. Neurosci.* **5**, 712–714 (2002).
20. Sjöström, P. J., Turrigiano, G. G. & Nelson, S. B. Rate, timing, and cooperativity jointly determine cortical synaptic plasticity. *Neuron* **32**, 1149–1164 (2001).
21. Wierenga, C. J., Walsh, M. F. & Turrigiano, G. G. Temporal regulation of the expression locus of homeostatic plasticity. *J. Neurophysiol.* **96**, 2127–2133 (2006).
22. Scott, D. N. & Frank, M. J. Adaptive control of synaptic plasticity integrates micro- and macroscopic network function. *Neuropsychopharmacol. Off. Publ. Am. Coll. Neuropsychopharmacol.* **48**, 121–144 (2023).
23. Martens, M. B., Celikel, T. & Tiesinga, P. H. E. A Developmental Switch for Hebbian Plasticity. *PLoS Comput. Biol.* **11**, e1004386 (2015).
24. Huang, C., Englitz, B., Reznik, A., Zeldenrust, F. & Celikel, T. *Information Transfer and Recovery for the Sense of Touch*. http://biorxiv.org/lookup/doi/10.1101/2020.12.08.415729 (2020) doi:10.1101/2020.12.08.415729.
25. Ching, S., Cimenser, A., Purdon, P. L., Brown, E. N. & Kopell, N. J. Thalamocortical model for a propofol-induced α-rhythm associated with loss of consciousness. *Proc. Natl. Acad. Sci.* **107**, 22665–22670 (2010).

26. Sherfey, J. S. *et al.* DynaSim: A MATLAB Toolbox for Neural Modeling and Simulation. *Front. Neuroinformatics* **12**, (2018).
27. Zeldenrust, F., Calcini, N., Yan, X., Bijlsma, A. & Celikel, T. The tuning of tuning: How adaptation influences single cell information transfer. *PLoS Comput. Biol.* **20**, e1012043 (2024).
28. Pospischil, M. *et al.* Minimal Hodgkin-Huxley type models for different classes of cortical and thalamic neurons. *Biol. Cybern.* **99**, 427–441 (2008).
29. Urbain, N. *et al.* Whisking-Related Changes in Neuronal Firing and Membrane Potential Dynamics in the Somatosensory Thalamus of Awake Mice. *Cell Rep.* **13**, 647–656 (2015).
30. Barth, A. L. & Poulet, J. F. A. Experimental evidence for sparse firing in the neocortex. *Trends Neurosci.* **35**, 345–355 (2012).
31. Benedetti, B. L., Glazewski, S. & Barth, A. L. Reliable and Precise Neuronal Firing during Sensory Plasticity in Superficial Layers of Primary Somatosensory Cortex. *J. Neurosci.* **29**, 11817–11827 (2009).
32. Voelcker, B., Pancholi, R. & Peron, S. Transformation of primary sensory cortical representations from layer 4 to layer 2. *Nat. Commun.* **13**, 5484 (2022).
33. Bi, G. Q. & Poo, M. M. Synaptic modifications in cultured hippocampal neurons: dependence on spike timing, synaptic strength, and postsynaptic cell type. *J. Neurosci. Off. J. Soc. Neurosci.* **18**, 10464–10472 (1998).
34. Petersen, C. C. H. The functional organization of the barrel cortex. *Neuron* **56**, 339–355 (2007).
35. Feldmeyer, D. *et al.* Barrel cortex function. *Prog. Neurobiol.* **103**, 3–27 (2013).
36. Azarfar, A., Calcini, N., Huang, C., Zeldenrust, F. & Celikel, T. Neural coding: A single neuron's perspective. *Neurosci. Biobehav. Rev.* **94**, 238–247 (2018).
37. Diamond, M. E., Huang, W. & Ebner, F. F. Laminar comparison of somatosensory cortical plasticity. *Science* **265**, 1885–1888 (1994).
38. Buonomano, D. V. & Maass, W. State-dependent computations: spatiotemporal processing

in cortical networks. *Nat. Rev. Neurosci.* **10**, 113–125 (2009).

39. Feldman, D. E. The spike-timing dependence of plasticity. *Neuron* **75**, 556–571 (2012).
40. Rolls, E. T. & Treves, A. The neuronal encoding of information in the brain. *Prog. Neurobiol.* **95**, 448–490 (2011).
41. Meissner-Bernard, C. *et al.* Computational functions of precisely balanced neuronal microcircuits in an olfactory memory network. *Cell Rep.* **44**, 115330 (2025).
42. Edelman, G. M. & Gally, J. A. Degeneracy and complexity in biological systems. *Proc. Natl. Acad. Sci. U. S. A.* **98**, 13763–13768 (2001).
43. Prinz, A. A., Bucher, D. & Marder, E. Similar network activity from disparate circuit parameters. *Nat. Neurosci.* **7**, 1345–1352 (2004).

Figures

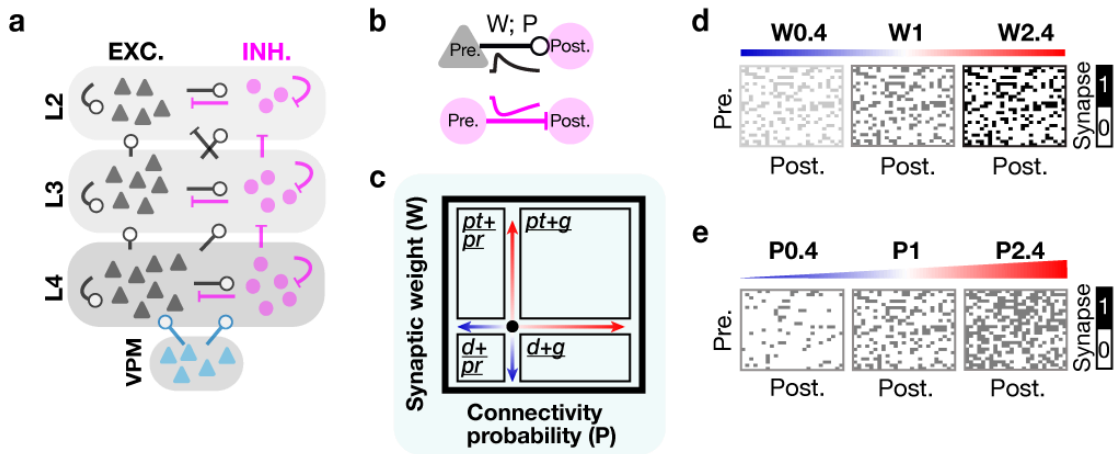

Figure 1: Studying metaplasticity in a multi-layer spiking neural network (mlSNN) model.

(**a**) The mlSNN architecture. Three cortical layers (L) contain excitatory (EXC., black triangles) and inhibitory (INH., pink circles) neurons. Layers have recurrent (within layers) and feedforward (between layers) connections (edges with circle tips, excitatory connections; pink edges with line tips, inhibitory connections). Both L4 populations receive activity patterns from excitatory neurons (blue triangles) in the thalamic ventral posteromedial (VPM) layer.

(**b**) Each edge (black, exc.; pink, inh.) from **a** has a specific weight (W) and probability (P). The black signal below the black edge shows the kinetics of the potential change in the postsynaptic (Post.) membrane caused by excitatory presynaptic (Pre.) activity. The pink signal on the pink edge shows postsynaptic change after inhibitory presynaptic activity.

(**c**) A cartoon of the experiment — a scaling of W and P in four directions with respect to the reference values P1 and W1 (black dot). Labels in quadrants — pt, potentiation; d, depression; g, growth; pr, pruning.

(**d**) Example realizations of connectivity matrices M for a random edge from **a**. We model plasticity in synaptic strength as a scaling of W. Scaling affects all existing synapses equally.

(**e**) Example realizations of connectivity matrices M for a random edge from **a**. We model plasticity in the number of synapses as a scaling of P, such that an increase of P adds synaptic connections of equal W to M, while a decrease of P removes synaptic connections. Synapses are removed and added randomly.

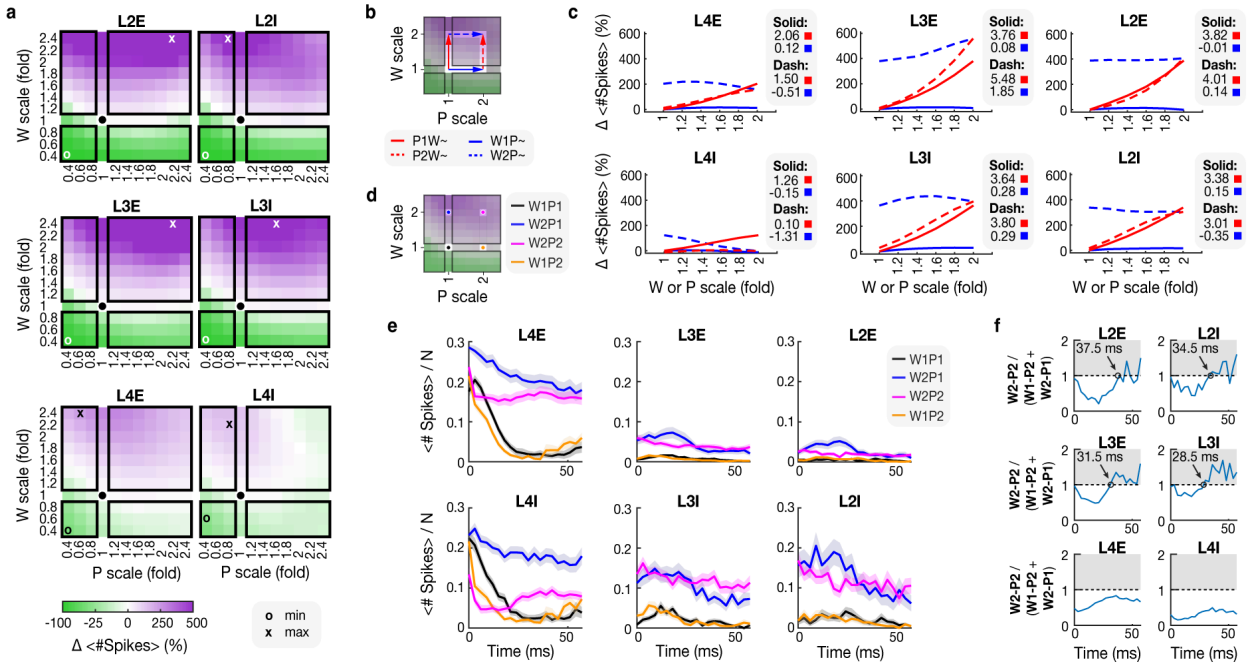

Figure 2: Modulation of spiking activity by changes in weights and probabilities, within and without metaplasticity.

(**a**) Relative change (%) in the mean spike number (#) with respect to W1P1 (black dots) is shown in color scale (below L4E, shared for all heatmaps) for six populations (in map titles). Synaptic weights (W, vertical axis) and numbers (P, horizontal axis) were scaled symmetrically (scaling factors: 0.4-2.4, increments of 0.2) to induce plasticity (W-P conditions between quadrants) and metaplasticity (conditions in quadrants). Symbols on maps point to conditions with the maximal positive change (x) and the minimal negative change (o). x and o are values in Table 1.

(b) A cartoon showing the four investigated network changes: solid lines, changes due to plasticity (red, influence of W given P1; blue, influence of P given W1); dashed lines, changes due to metaplasticity (red, influence of W given P2; blue, influence of P given W2).

(**c**) Relative change (%) in the mean spike number in the four transition conditions outlined in **b**. Line legend (color, style) is shown in **b**. Population names are above the panels. The slope of every transition trajectory is reported on the right of every population panel. Top two values are for “Solid” lines, and the bottom two values are for “Dash” lines.

(**d**) A cartoon showing the networks analysed in **e**: black dot, initial network (i.e., no plasticity); orange dot, initial weights (W1) doubled probabilities (P2); blue dots, doubled

weights (W2) initial probabilities (P1); pink dot, doubled weights and probability (W2P2). See legend on the right.

(**e**) The temporal evolution of the mean spike number normalized by the population size (<#Spikes>/N; mean in solid ± SEM in shade) for the networks in **d** (coloured dots) for all populations (names in titles). Activity is measured from the peak in thalamic population spiking (i.e., input onset, set at 0 ms) to 60 ms post-onset (bin size, 3 ms). Line legend in L2E is shared for all panels and matched networks in **d**.

(**f**) Linearity of the interaction between the effects of W and P plasticity on the population-averaged spiking activity (S). The difference between the activity in the metaplasticity condition (W2P2, pink in **e**) was compared to the combined effect of the two plasticity conditions (W1P2 (orange) and W2P1 (blue) in **e** by dividing the combined activity by the sum of the two separate effects: $S_{W2\text{-}P2}$ / ($S_{W1\text{-}P2}$+$S_{W2\text{-}P1}$). Grey area: supralinear W-P interaction; white area: sublinear W-P interaction. Black circle: switch from sub- to supra-linearity. Black values: switching latency.

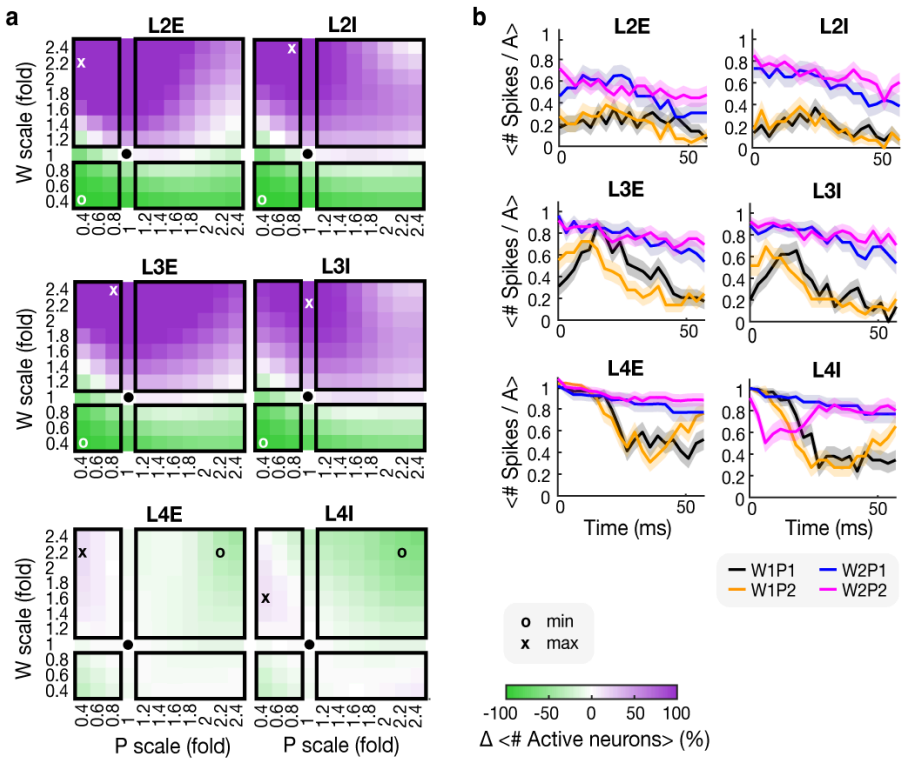

Figure 3: Resizing of the pool of active neurons and changes in their temporal dynamics under (meta)plasticity.

(**a**) Relative change (%) in the average number of active neurons per pattern with respect to W1P1 (black dots) is shown in color scale (right from L4I, shared for all heatmaps) for six populations (in titles) for networks from Figure 2a. Scaling of W, vertical axis; scaling of P, horizontal axis. Symbols on maps point to conditions with the maximal positive change (x) and the minimal negative change (o). x and o are values in Supplementary Table 7.

(**b**) The temporal evolution of activity divided by the number of active neurons per bin ($N_{A,\ bin}$; mean in solid ± SEM in shade) from the network settings in Figure 2e (see legend below L4I panel). The activity is measured from the input pattern onset (0 ms) to 60 ms post-onset (bin size, 3 ms). Population names are above panels. Legend is shared for all panels.

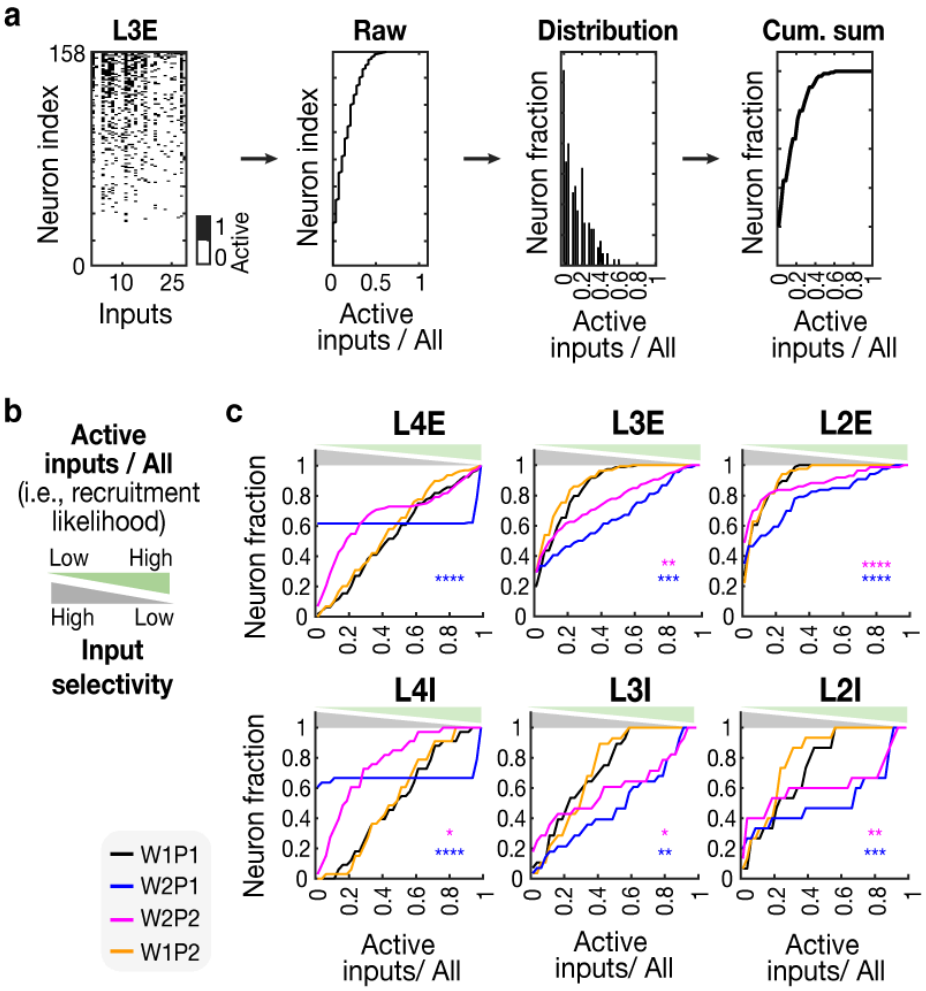

Figure 4: Population-wide changes in distributions of input selectivities following (meta)plasticity.

(**a**) Illustration of the quantification of input selectivity distribution within one population in **b**: first box, example responses of L3E neurons (vertical axis) to 30 inputs (horizontal axis, Online Methods). Black dots, inputs for which a specific neuron is active; white, inputs for which a specific neuron is inactive. Second box: fraction of inputs evoking activity (horizontal axis) for all neurons in L3E (vertical axis). Third box: fraction of neurons (vertical axis) across active input fractions (horizontal axis) from the second box. Fourth box: cumulative sum of the distribution from the third box.

(**b**) Fraction of inputs that evoked activity (Active patterns / All) reflects the likelihood of neurons to be recruited into the active pool (green scale) and is reversely proportional to pattern selectivity (gray scale). This relationship is superimposed on plots in **c**.

(**c**) Cumulative distributions (as in **a**) of active-input fractions (horizontal axis) per population (in titles) from four networks (legend left from L4I panel — black, W1-P1; orange, W1-P2; blue, W2-P1; pink, W2-P2 condition). W1P1 condition was statistically compared to the three non-black conditions: asterisk (bottom right corner) color is marked significance for the color-matching condition. Kolmogorov-Smirnov test with Bonferroni correction for multiple comparisons (*, $p<0.05$; **, $p<0.01$; ***, $p<0.005$; ****, $p<0.001$).

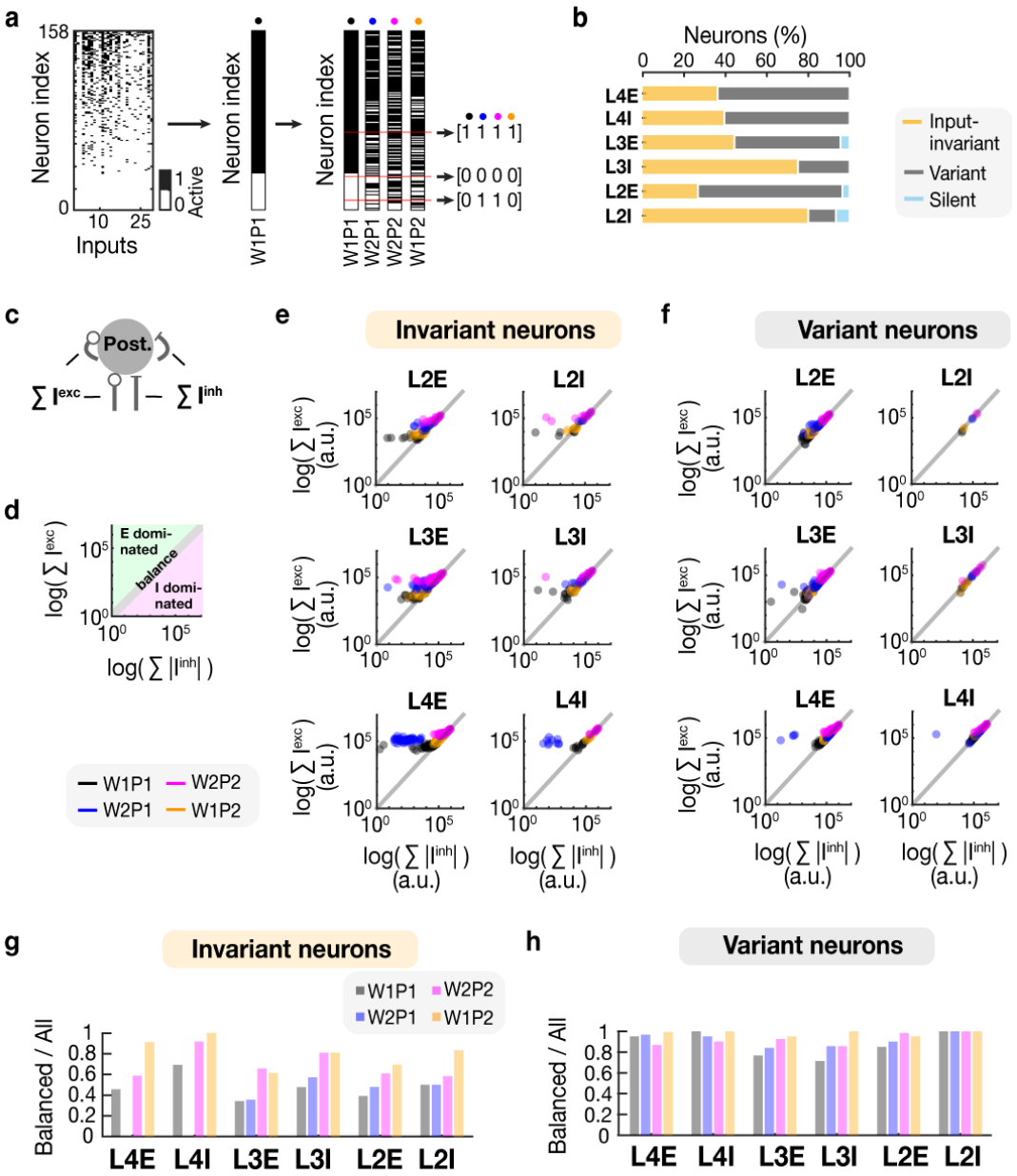

Figure 5: Mechanistic dissection of heterogeneity in neuronal subtypes pre- and post-(meta)plasticity.

(a) Illustrated example of the classification protocol behind data in b. Left side, inputs (horizontal axis, Online Methods) presented to the network triggered activity (black points) in neurons (vertical axis). Middle, activity from the population from left represented as a binary vector: neurons responsive to ≥ 1 input get assigned a 1 (black) 0 otherwise (white). Right side, four binary vectors represent the same population (left) across four different conditions (see dots on top or labels below each vector): black, W1-P1; orange, W1-P2; blue, W2-P1; pink, W2-P2. Numbers on the right: classification protocol with three categories (examples shaded with red lines): (1) neurons responsive in all four conditions (code: 1111, label: input-invariant),

(2) neurons inactive in all four conditions (code: 0000, label: silent) or (3) neurons with mixed responsiveness (e.g. code: 0110, label: variant).

(**b**) Percentage (%) of neurons (horizontal axis) in each class from **a** for all six populations (horizontal bars). Invariant (orange): neurons responsive in all four conditions; silent (blue): neurons with no activity in four conditions; variant (grey): neurons with mixed responsiveness.

(**c**) Illustration of the analysis behind data in **e-f**: the sums of all excitatory ($\sum I^{exc}$) and inhibitory ($\sum I^{inh}$) presynaptic inputs collected per postsynaptic neuron.

(**d**) Relationship between $\sum I^{exc}$ (vertical axis) and $|\sum I^{inh}|$ (horizontal axis) from **e** represented on a log-log plane, where data on the diagonal suggests an E-I balance, above the diagonal an E-dominated state and below the diagonal an I-dominated state.

(**e**) For each invariant neuron (orange fractions in **b**), the sum of all excitatory and inhibitory currents are shown for the four conditions: black, W1P1; blue, W2P1; pink, W2P2; orange, W1P2.

(**f**) Same as in **e** but for variant neurons (grey fractions in **b**).

(**g**) Fraction of invariant neurons (vertical axis) on the “balance” diagonal ($-0.5 < \log(\sum I^{exc} / |\sum I^{inh}|) < 0.5$) in **e** per population (horizontal axis).

(**h**) Same as in **g** but for variant neurons from **f**.

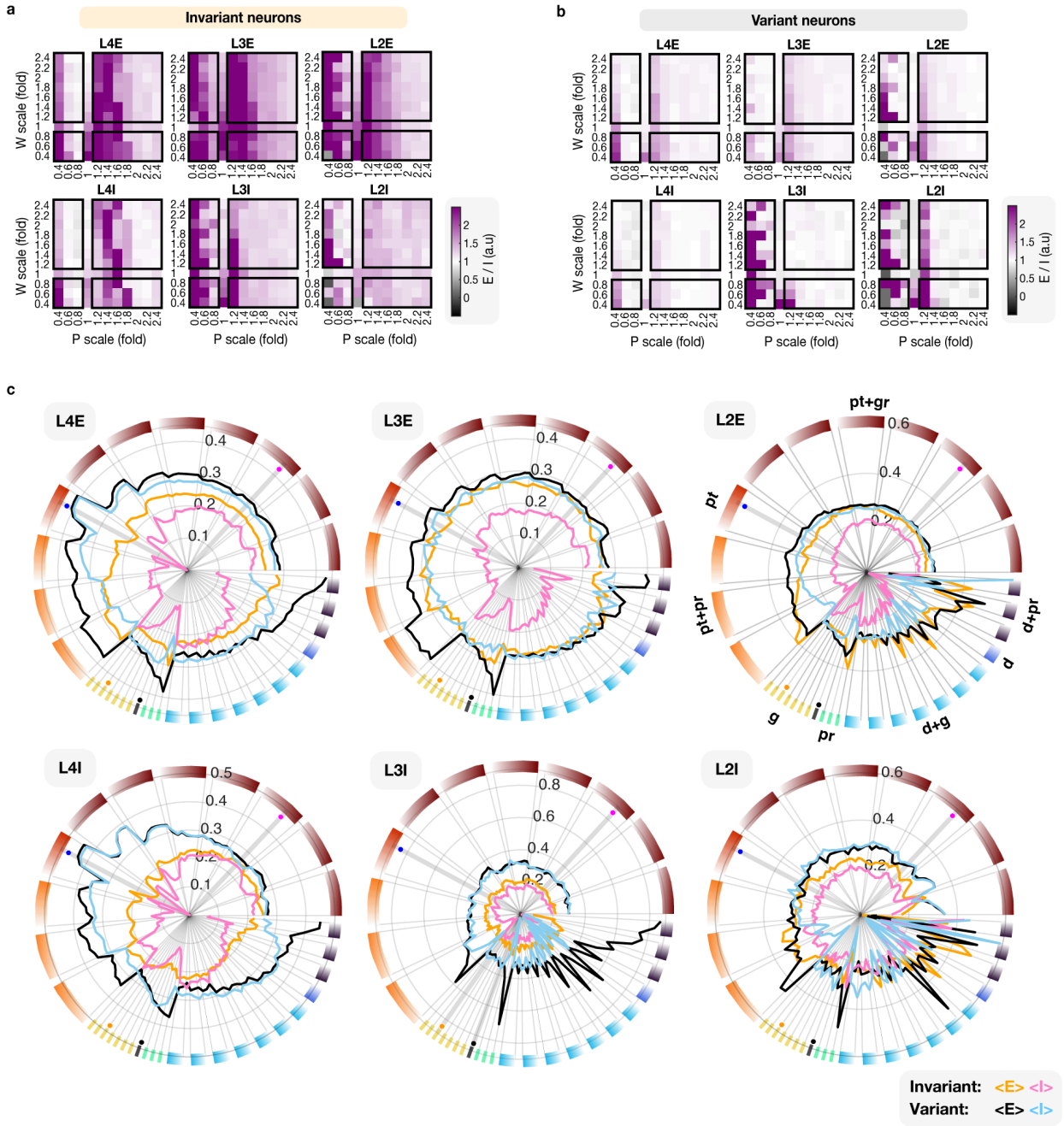

Figure 6: The emergence of E-I balance and the sensitivity of E and I presynaptic currents to metaplasticity-dependent changes in input-invariant and variant neuronal subtypes.

(a) In invariant neurons (Figure 5b), the ratio of relative excitation (E) and inhibition (I) in six populations (titles above maps) as W and P are scaled (vertical and horizontal axes, respectively). W-P conditions with a ratio ≈ 1 (white) show the emergence of E-I balance.

(**b**) Same as in **a** but for variant neurons.

(**c**) A circular representation of presynaptic currents for each population. Population titles are in the top left of each circle (data arrangement steps are in Supplementary Figure 6a). In the L2E panel (top right), see abbreviations for orientation (pt, potentiation; d, depression; g, growth; pr, pruning). The four networks in the previous focus are shown in dots — black, W1-P1; orange, W1-P2; blue, W2-P1; pink, W2-P2 condition. Relative currents for invariant neurons from Figure 5b are in orange (excitatory, E) and pink (inhibitory, I). For variant neurons from Figure 5b, currents are in black (excitatory) and blue (inhibitory). See the legend in the bottom right.

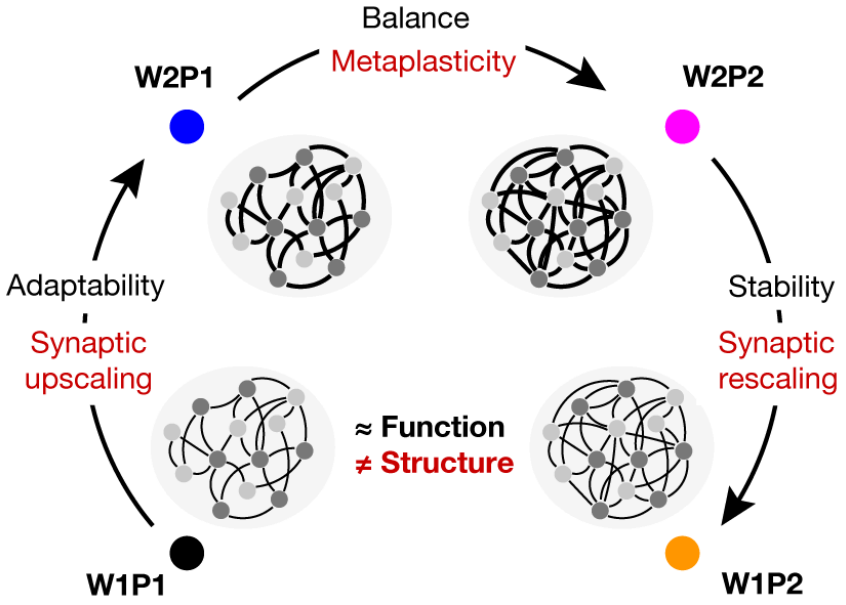

Figure 7: The Proposed Continuum of Plasticity Mechanisms to Establish Functional Homeostasis. The continuum of network states (W1P1 → W2P1 → W2P2 → W1P2) illustrates how synaptic upscaling (W>1, W2P1) drives adaptability via elevated activity, while synaptic rescaling (W=1, W1P2) stabilizes the network through metaplasticity. Despite persistent structural remodelling (W1P1 ≠ W1P2), functional outputs return to baseline (W1P1 ≈ W1P2), demonstrating functional homeostasis. Metaplasticity orchestrates this balance by non-linearly integrating W and P adjustments (Figures 3a, 4c, 5g), enabling robust functional homeostasis amid structural divergence.

1 Methods

1.1 Modelling.

Cortical neuron model. We model single-compartment spiking neurons using the Hodgkin-Huxley formalism. The membrane potential V_i of neuron i evolved over time (t) as

$$C_m \dot{V}_i = -\sum_k I_k(t) + \sum_{syn} I_{syn}(t) + I_i(t), \quad (1)$$

where C$_m = 1\mu F/cm^2$ was the membrane capacitance, $\sum_k I_k$ was the sum of ionic currents passing through the voltage-gated channels k, $\sum_{syn} I_{syn}$ was the sum of ionic currents passing through postsynaptic receptors syn (see Paragraph 1.1) and $I_i(t)$ was the neuron-specific time-varying noise current

$$I_i(t) = \sqrt{dt}\sigma\xi_i(t), \quad (2)$$

where $dt = 0.01$ ms was the simulation time step, ξ_i was a random value drawn independently at every simulation step for every neuron i from a Gaussian distribution with mean μ = 0 and unit standard deviation scaled by σ = 100 pA/$\sqrt{ms}$.

The following ionic channel currents k were used in $\sum_k I_k$ (Eq. (1)), taken from predefined minimal Hodgkin-Huxley models for sensory cortical excitatory (E) and inhibitory (I) neurons by (Pospischil et al., 2008):

$$\sum_k I_k = I_{Na} + I_{KDR} + I_M + I_L, \quad (3)$$

where the sodium (Na) current was used to model neuronal depolarization, delayed corrected potassium (KDR) was used for repolarization, slow non-inactivating potassium (M) was used for hyperpolarization, and leak (L) current was used to maintain baseline polarization. Below are equations from (Pospischil et al., 2008), and see Supplementary Table 1 for parameter values.

The sodium channel current evolved as

$$I_{Na} = g_{Na} m^3 h(V - E_{Na}), \quad (4)$$

where g_{Na} was the maximum channel conductance, E_{Na} was the channel reversal potential, and m and n were the channel activation and inactivation variables, respectively, such that

$$\dot{m} = \alpha_m(V)(1-m) - \beta_m(V)m \quad (5)$$

$$\dot{h} = \alpha_h(V)(1-h) - \beta_h(V)h, \quad (6)$$

where α was the transition rate from open to closed channel conformation, and β was the transition rate from open to closed conformation. Both α and β depended on the fixed threshold potential V_T such that

$$\alpha_m = \frac{-0.32(V - V_T - 13)}{\exp[\frac{-(V-V_T-13)}{4}] - 1}, \quad (7)$$

$$\beta_m = \frac{0.28(V - V_T - 40)}{\text{exp}[\frac{-(V-V_T-40)}{5}] - 1}, \quad (8)$$

$$\alpha_h = 0.128\,\text{exp}[\frac{-(V - V_T - 17)}{18}], \quad (9)$$

$$\beta_h = \frac{4}{1 + \text{exp}[\frac{-(V-V_T-40)}{5}]}. \quad (10)$$

The delayed-rectified channel current evolved as

$$I_{KDR} = g_{KDR} n^4 (V - E_{KDR}), \quad (11)$$

where g_{KDR} was the maximum channel conductance, E_{KDR} was the channel reversal potential, and n represented the channel activation variable such that

$$\dot{n} = \alpha_n(V)(1 - n) - \beta_n(V)n, \quad (12)$$

with α as the closed-to-open transition rate, β open-to-closed transition rate, and V_T being the fixed threshold such that

$$\alpha_n = \frac{-0.032(V - V_T - 15)}{\text{exp}[\frac{-(V-V_T-15)}{5}] - 1}, \quad (13)$$

$$\beta_n = 0.5\,\text{exp}[\frac{-(V - V_T - 10)}{40}]. \quad (14)$$

The slow non-inactivation channel current evolved as

$$I_M = g_M p (V - E_M), \quad (15)$$

where g_M is the maximum channel conductance, E_M is the channel reversal potential, and p is the channel activation variable which evolves as

$$\dot{p} = \frac{p_\infty(V) - p}{\tau_p(V)}, \quad (16)$$

where p_∞ was its steady-state activation function, given by

$$p_\infty = \frac{1}{1 + \text{exp}[\frac{-(V+35)}{10}]}, \quad (17)$$

and τ_p was the channel time constant, which depended on the fixed variable τ_{max} as

$$\tau_p = \frac{\tau_{max}}{3.3\,\text{exp}[\frac{V+35}{20}] + \text{exp}[\frac{-(V+35)}{20}]}. \quad (18)$$

The leak channel current evolved as

$$I_{leak} = g_{leak}(V - E_{leak}), \quad (19)$$

where g_{leak} was the maximum channel conductance and E_{leak} was the channel reversal potential.

Cortical neuron model fitting. Pospischil et al. (2008) distinguish between E and I neurons using channel-specific parameter values to capture known differences in their input-output characteristics. In the primary somatosensory cortex (barrel, S1) in rodents, E neurons emit action potentials (APs, spikes) at a lower frequency than I neurons when triggered by a current injection with identical amplitude (Zeldenrust et al., 2024). In our simulation of the current-frequency

(I-f) experiment detailed in Figure 1F of Zeldenrust et al. (2024), we applied current pulses of constant duration (500 ms) and varying amplitude (ranging from 0 to 400 pA, in 40 pA increments) to E (Supplementary Figure 7a) and I (Supplementary Figure 7b) neurons modelled after (Pospischil et al., 2008). We found that the I-f curves for the empirically measured E and I neurons did not match those of the modelled neurons (Supplementary Figure 7c). Therefore, we adjusted g_{Na}, g_M, g_{leak}, V_T and τ_{max} from Pospischil et al. (2008) for a closer match in I-f properties between the empirical E and I neurons from (Zeldenrust et al., 2024) and E and I models from (Pospischil et al., 2008). The E and I neurons used in our network model have adjusted values reported in Supplementary Table 1.

Thalamic neuron model. We defined excitatory thalamocortical relay (TCR) neurons as single-compartment Hodgkin-Huxley models where the membrane potential V of neuron i evolved over time t as

$$\dot{V}_i = -\sum_k I_k(t) + I_{ext}(t). \tag{20}$$

where $\sum_k I_k$ was the sum of ionic currents passing through the voltage-gated channels k and I_{ext} was the external input current specific to the neuron, used to trigger its spiking activity. A comprehensive definition of I_{ext} (Eq. (49)) will be provided in the section on thalamic population stimulation below.

We used the following ionic currents k from the TCR neuron model of Ching et al. (2010):

$$\sum_k I_k = I_{Na} + I_K + I_T + I_h + I_{K-L} + I_L. \tag{21}$$

Here, the sodium (Na) current evolution was given by

$$I_{Na} = g_{Na} m^3 h (V - E_{Na}), \tag{22}$$

where g_{Na} = 90 mS was the maximum channel conductance, E_{Na} = 50 mV was the channel reversal potential, while m and n represent the channel activation and inactivation variables, respectively, such that

$$\dot{m} = \alpha_m(V)(1-m) - \beta_m(V)m, \tag{23}$$

$$\dot{h} = \alpha_h(V)(1-h) - \beta_h(V)h, \tag{24}$$

with α as the closed-to-open transition rate constant and β open-to-closed transition rate. These were defined as

$$\alpha_m(V) = \frac{0.32(13 - V + V_T)}{\exp[(13 - V + V_T)/4] - 1} \tag{25}$$

$$\beta_m(V) = \frac{0.28(V + V_T - 40)}{\exp[(V + V_T - 40)/5] - 1} \tag{26}$$

$$\alpha_h(V) = 0.128\,\text{exp}[(17 - V + V_T)/18] \quad (27)$$

$$\beta_h(V) = \frac{4}{1 + \text{exp}[(40 - V + V_T)/5]}, \quad (28)$$

with the fixed threshold V_T = 35 mV.

The potassium (K) current evolution was described by

$$I_K = g_K m^4 (V - E_K), \quad (29)$$

where g_K 10 mS, was the maximum channel conductance, E_K -100 mV was the channel reversal potential, and m represented the channel activation variable, such that

$$\dot{m} = \alpha_m(V)(1 - m) - \beta_m(V)m, \quad (30)$$

with α as the closed-to-open transition rate constant and β open-to-closed transition rate, defined as

$$\alpha_m(V) = \frac{0.032(15 - V + V_T)}{\text{exp}[(15 - V + V_T)/5] - 1} \quad (31)$$

$$\beta_m(V) = \frac{0.5(10 - V + V_T)}{\text{exp}[(10 - V + V_T)/40]}, \quad (32)$$

with fixed threshold V_T = 25 mV.

Next to the standard sodium and potassium currents, thalamic neurons had a T-type calcium channel current, which was described by

$$I_T = g_{Ca} m_\infty^2 h (V - E_{Ca}), \quad (33)$$

where g_{Ca} = 2 mS was the maximum channel conductance, E_{Ca} = 120 mV was the channel reversal potential, m represented the channel activation which evolved to its steady state m_∞:

$$m_\infty = \frac{1}{(1 + \text{exp}[-(V + V_T + 57)/6.2])} \quad (34)$$

and similarly h represented the inactivation variable, which evolved to steady state h_∞

$$\dot{h} = (h_\infty - h)/\tau_h, \quad (35)$$

based on

$$h_\infty = \frac{1}{(1 + \text{exp}[(V + V_T + 81)/4])} \quad (36)$$

with a time constant

$$\tau_h = (30.8 + (211.4 + \text{exp}[(V + V_T + 113.2)/5])/(1 + \text{exp}[(V + V_T + 84)/3.2]))/3.72. \quad (37)$$

Both m and h depended on a fixed threshold V_T = 2 mV.

The TCR neuron also had a hyperpolarisation-activated h-current, whose

dynamics were described by

$$I_h = g_h(o_1 + 2(1 - c_1 - o_1))(V - E_h), \quad (38)$$

where g_h was the maximum channel conductance (Supplementary Table 2), E_h = -40 mV was the channel reversal potential, o_1 was the channel activation variable and c_1 was the channel inactivation variable. The activation variable o_1 was modelled as

$$\dot{o_1} = 0.001(1 - c_1 - o_1) - 0.001((1 - p_0)/0.01), \quad (39)$$

where p_0 modulated the h-current as

$$\dot{p_0} = 0.0004(1 - p_0) - 0.0004([Ca]_i/0.002)^4, \quad (40)$$

based on the intracellular calcium concentration ($[Ca]_i$) which was modelled as

$$[\dot{Ca}]_i = \frac{-10I_T}{2 * 96489} + \frac{0.00024 - [Ca]_i}{5}. \quad (41)$$

The inactivation c_1 was defined as

$$\dot{c_1} = \beta(V)o_1 - \alpha(V)c_1, \quad (42)$$

where α and β were the voltage-dependent rate constants for the closed-to-open and open-to-closed conformation transitions, respectively:

$$\alpha(V) = h_\infty(V)/\tau_s(V), \quad (43)$$

$$\beta(V) = (1 - h_\infty(V))/\tau_s(V), \quad (44)$$

where h_∞ was the steady-state variable and τ_s was its time constant such that

$$h_\infty(V) = \frac{1}{1 + \text{exp}[(V + 75)/5.5]}, \quad (45)$$

$$\tau_s(V) = 20 + 1000/((1 + \text{exp}[(V + 71.5)/14.2]) + (1 + \text{exp}[-(V + 89)/11.6])). \quad (46)$$

The TCR neuron had two leak channels, a potassium (K_leak) and a general (leak) channel, which were described by

$$I_{K_leak} = 0.0172(V + 100) \quad (47)$$

and

$$I_{leak} = 0.01(V + 70). \quad (48)$$

Thalamic neuron model fitting. As described above, the TCR model was taken from Ching et al. (2010), were authors reproduced spiking activity during anaesthesia. In this state, TCR neurons are hyperpolarized and produce bursts of activity upon stimulation

(Supplementary Figure 7d,e). To simulate thalamic spiking in awake as opposed to anaesthetised states, we depolarized the resting membrane potentials of TCR neurons by increasing the maximal conductance of the hyperpolarization-activated h-current g_h. We modelled two thalamic subpopulations in our network, whose properties will be discussed in the next section, for which we increased g_h separately. Furthermore, we increased the external input strength g_{in} (Eq. (49)) and decreased the input frequency for each thalamic subpopulation, see Supplementary Table 2 for original and adjusted values. The parameter adjustments rescued the thalamic activity from bursting, such that it showed single spikes at high rates (Supplementary Figure 7d), similar to thalamic spiking during active whisking in rodents (Urbain et al., 2015).

Structured thalamic input to cortex. To control input into cortical L4, we defined two thalamic subpopulations: pattern-generating (Supplementary Figure 7f) and background (Supplementary Figure 7g) TCR neurons (combined in Supplementary Figure 7h). Both subpopulations were stimulated with an external current I_{ext} (Eq. (20)), derived from a Poisson spike train as discussed later in this section. For the pattern-generating neurons, I_{ext} was designed such that the neurons spiked synchronously, to increase the population spike count within a limited time window (minimum of 10 spikes in 3 ms time bin; Supplementary Figure 7i, red line) which constituted a "pattern" of activity that propagated across cortical layers (Supplementary Figure 1a). The input current I_{ext} of background spiking neurons was designed to trigger asynchronous activity. We described the generation of I_{ext} below.

For both populations, the external input current I_{ext} that drives spiking in TCR neurons (Eq. (20)), was modelled as

$$I_{ext}(t) = \frac{g_{in}}{N} \odot Ge(t) \odot M \odot (V(t) - E_{in}), \quad (49)$$

where g_{in} was the maximal conductance of the input (0.01 mS/cm^2 for pattern-generating neurons; 0.005 mS/cm^2 for background neurons), E_{in} = 1 mV was the reversal potential of the input and N was the number of neurons (45 pattern-generating; 24 background). N was arbitrary. Ge was a matrix of size $N \times T$ with N time-varying inputs of length T, where T was the number of time steps equal to the simulation duration (600 ms) divided by dt (0.01 ms). M was a column vector with N rows, each with a binary value of 0 or 1. The number of positive elements (1) in M was constrained by the probability P_{In} (0.3 for pattern-generating; 0.1 for background). When multiplied with Ge, M controlled which neurons received the external input contained in Ge such that the neuron i received the input from the i-th row in Ge if the i-th row in M was 1. The generation of N neuron-

specific inputs in Ge will be explained below. We used the Hadamard product $\odot$ for element-wise operations on vectors and matrices.

To generate Ge for the pattern-generating thalamic subpopulation, we first created a template signal with binary values in which ones randomly occurred at times t_s, where t_s were generated by a Poisson process with rate r = 9 Hz. For every row in Ge, we jittered each t_s independently by adding a randomly drawn time shift from the Gaussian distribution (μ=0; σ=5 ms). We used a double exponential kernel x (Eq. (50)) defined below to convolve rows in Ge to mimic the naturalistic excitatory postsynaptic potential (EPSP) kinetics.

To generate Ge for background thalamic spiking, we created a unique binary template for each row in Ge, where ones occured at times t_s generated by a Poisson process with rate r = 12 Hz. The templates were then also convolved with x.

The kernel x was described as

$$x(t) = \alpha \frac{\text{exp}(\frac{-t}{\tau_d}) - \text{exp}(\frac{-t}{\tau_r})}{(\tau_d - \tau_r)}. \quad (50)$$

where α (14 pA for pattern-generating; 25 pA for background) scaled the EPSP amplitude and τ_r = 0.5 ms and τ_d = 2 ms were the rise and decay time constants, respectively.

Synapse model. Cortical neurons received a combination of excitatory and inhibitory synaptic currents I_{syn} (Eq. (1)) such that

$$\sum_{syn} I_{syn}(t) = I_{AMPAR}(t) + I_{GABAaR}(t) \quad (51)$$

where AMPAR was the excitatory α-amino-3-hydroxy-5-methyl-4-isoxazolepropionic acid receptor and GABAaR was the inhibitory γ-aminobutyric acid type-a receptor. The receptor-specific currents were modelled as

$$I_{AMPAR} = g_{AMPAR} \odot A_{AMPAR}(t) \odot M_{AMPAR} \odot (V(t) - E_{AMPAR}), \quad (52)$$

and

$$I_{GABAaR} = g_{GABAaR} \odot A_{GABAaR}(t) \odot M_{GABAaR} \odot (V(t) - E_{GABAaR}), \quad (53)$$

where g_{AMPAR} and g_{GABAaR} were the maximum channel conductances, E_{AMPAR} and E_{GABAaR} were the channel reversal potentials, $A_X(t)$ was the activation function (Eq. (54)) and M_X the connectivity matrices with weights (W) and numbers of synapses constrained by a probability (P); W and P were specific for every pre-to-postsynaptic population pair (see Supplementary Table 5 and the paragraph below for the generation of connectivity matrices M).

To normalize E and I currents before imposing synapse-specific weights, we scaled g_{AMPAR} and g_{GABAaR} to match the amplitudes of unitary E and I postsynaptic potentials (uEPSP and uIPSP, respectively) evoked by 1 presynaptic action potential. The range of uEPSP and uIPSP amplitudes for synapses in cortical layers (L) 4 and 2/3 was between ∼0.5 and ∼7 mV (Markram et al., 2015). The amplitudes in our model were matched at ∼2.3 mV which is within the expected range.

The g_{AMPAR} for thalamocortical synapses was doubled compared to cortical g_{AMPAR} to account for the size difference between the pattern-generating thalamic subpopulation and the input-receiving cortical L4 (Supplementary Tables 2 and 4): this way the activation of cortical L4 neurons after thalamic spiking was ensured. See Supplementary Table 3 for values of all conductance parameters.

The activation function $A(t)$ in Eqs. (52, 53) was defined as

$$\dot{A_X} = [(\frac{-A}{\tau_{decay}}) + (\frac{1-A}{\tau_{rise}})(1 + \tanh(\frac{V_{presyn}}{10}))]/2 \quad (54)$$

were X was either AMPAR or GABAaR, τ_{rise} and τ_{decay} were the rise and decay time constants respectively (Supplementary Table 3), and V_{presyn} was the membrane potential of a presynaptic neuron.

Network size and connectivity. The E and I cortical neurons were distributed in three layers: L4, L3 and L2, which follow the same laminar organisation as observed in rodent S1. The layer sizes were set to 5% of the average layer-specific neuron number in a single rat cortical column reported in (Meyer et al., 2010) which resulted in 221 neurons in L4, 181 in L3 and 101 in L2. We then applied the 85-to-15% E-to-I neuron ratio to determine the number of excitatory and inhibitory neurons per layer (Supplementary Table 4).

There were 69 thalamic neurons in total; 45 were used to generate input patterns, while the remaining 24 produced background activity. The population sizes were set arbitrarily to model the desired population spiking dynamics.

Synaptic connectivity between the presynaptic and postsynaptic populations was implemented in the matrix M (Eqs. 52 and 53). Each matrix M was parameterized by two values: (1) synaptic weight (W), defining connection strength, and (2) fixed probability (P), defining the number of existing synapses. Connection-specific W and P values were derived from (Markram et al., 2015): we used the values for "synapse count" to define W and "connection probability" to define P (Supplementary Table 5). Our network contained 21 unique synapses identifiable based on the pre- and post-labels (e.g., L4E →L4I; Supplementary Table 3, edges in Figure 1a).

For each M, the total number of synapses

Syn was calculated as:

$$Syn = N_{\text{pre}} \times N_{\text{post}} \times P, \tag{55}$$

where N_{pre} and N_{post} were the presynaptic and postsynaptic population sizes, respectively. We initialized M as a sparse binary matrix ($N_{\text{pre}} \times N_{\text{post}}$) and randomly assigned S active synapses ($M_{ij} = 1$). Synaptic weights were then applied via element-wise multiplication of M by W.

Simulations. The model was constructed and simualted with Dynasim (Sherfey et al., 2018) in Matlab. Each network realization was simulated for 600 ms, with dt = 0.01 ms and the 4th-order Runge-Kutta ODE solver. Due to initial settling effects, the initial 100 ms of network activity was excluded from analyses (Supplementary Figure 1a).

Plasticity and metaplasticity experiments. To model (meta)plasticity in the network, we systematically scaled W and P across a symmetric 2D parameter space with a shared vector of scaling factors. Scaling factors were ranging from 0.4 to 2.4 (in 0.2 increments) and were chosen arbitrarily. For each (meta)plasticity condition $WxPy$, x and y scaled W and P, respectively, relative to their connection-specific baseline values. Baseline values were unscaled in the W1P1 condition, which represented the initial network state, i.e. the no-plasticity condition.

We simulated all x-y combinations which resulted in 121 $WxPy$ conditions, each repeated 10 times for 600 ms. When either x or y were 1 (i.e., unscaled), we consider that to be the expression of plasticity, in constrast to metaplasticity – when both W and P were scaled (i.e., x and y ≠ 1).

Variability origins in the model. All network simulations were performed under the fixed simulation seed ($rng(49)$ in Matlab) to ensure replicability of the random structure in connectivity matrices M (Eq. (52 and 53)) across the full dataset. Fixing the seed resulted in a "deterministic" random number generation for the time-varying noise we added to cortical neurons ($I_i(t)$ in Eq. 1) such that it was identical in all network realizations. Therefore, the whole cortical structure of the network, including thalamocortical connectivity matrices, was a fixed system.

The origin of the variability in the model was constrained to the thalamic population level. For each network realization, we let Ge (Eq. 49) vary randomly, driven by the Poisson process. This led to various thalamic neurons producing distinct input patterns, which occurred randomly across different network realizations, driving variability in cortical responses.

1.2 Analysis.

Isolating cortical activity for analysis. Cortical populations responded to continuous tha-

lamic activity which we thresholded to detect discrete events. Post-simulation, we looked for peaks in thalamic activity histogram (spikes sorted in 3 ms time bins) larger than 1.5$\times$ SD (standard deviation; usually 10 spikes/bin). We then chose the window boundaries t_1 (left) and t_2 (right) so that t_1 is aligned with the onset of the peak thalamic activity and t_2 is the time at which all cortical populations decay to baseline after the event-triggered activity.

Our exploratory analysis (Supplementary Figure 1d) showed that L4 populations respond the fastest and decay within 20 ms post-peak onset, while L2 populations had the longest response latency (full decay to baseline at 60 ms post-peak onset). Therefore $t_2 = t_1 + 60$ ms. We used the 60 ms window to isolate cortical spiking triggered by all detected thalamic peaks. Since different thalamic neurons contribute to population spiking per each event, we considered every detected event as a specific input pattern. A few example inputs are shown in Supplementary Figure 1c.

Spiking averages. In Figure 2a, we reported the relative change in the number of spikes per population averaged over K thalamic inputs. First, we obtained average spiking in a population as

$$S^{pop}_{WxPy} = \frac{1}{K}\sum_{k=1}^{K}\sum_{i=1}^{N} x_i, \qquad (56)$$

where x_i was the sum of all spikes from neuron i within $[t_1^k, t_2^k]$ for k-th input, summed across all neurons (N) in the population. S^{pop} was calculated for every $WxPy$ condition. Finally, we normalized all S^{pop}_{WxPy} to the W1P1 condition specific to each population and calculated the relative change

$$\Delta S^{pop}_{WxPy} = \frac{(S^{pop}_{WxPy} - S^{pop}_{W1P1})}{S^{pop}_{W1P1}} \times 100. \qquad (57)$$

Relative ΔS^{pop}_{WxPy} values were sorted in matrices (rows with fixed Wx, columns with fixed Py) which we smoothed applying the 2-D Gaussian smoothing kernel to each matrix M^{pop} using the *imgaussfilt(M, σ)* function in Matlab, where σ = 1.5 specified the standard deviation of the square kernel. The Gaussian kernel G was defined:

$$G(x,y) = \frac{1}{2\pi\sigma^2} exp(-\frac{x^2+y^2}{2\sigma^2}). \qquad (58)$$

which resulted in the smoothed matrix M'^{pop}:

$$M'^{pop}(x,y) = (M^{pop} * G)(x,y) \qquad (59)$$
$$= \sum_{m=-k}^{k}\sum_{n=-k}^{k} M(x-m, y-n)G(m,n)$$

where k = 5 was half the kernel size.

In Figure 2c, we used data from the smoothed matrices, focusing exclusively on values related to WxPy conditions, where x and y ranged from

1 to 2. From each M'^{pop}, we extracted four vectors: solid blue lines, Δ_{WxPy} values for $x = 1$ and y ranging from 1 to 2 (step size = 0.2); dashed blue lines, Δ_{WxPy} values for $x = 2$ and y ranging from 1 to 2; solid red lines, Δ_{WxPy} values for $y = 1$ and x ranging from 1 to 2; dashed red lines, Δ_{WxPy} values for $y = 2$ and x ranging from 1 to 2. We used linear regression to obtain the slope for each of the four vectors (slopes reported in Figure 2c).

In Figure 2e, we reported averaged spiking in time, normalized to the population size (N) as

$$S^{pop}_{WxPy}(t) = \frac{1}{K}\sum_{k=1}^{K}\frac{1}{N}\sum_{i=1}^{N} x_i(t), \qquad (60)$$

where $x_i(t)$ is the sum of spikes from neuron i in the time bin t (bin size = 3 ms). In Figure 2f, we used spiking in time to determine population-specific linearity $L^{pop}(t)$ as

$$L^{pop}(t) = \frac{S^{pop}_{W2P2}(t)}{(S^{pop}_{W1P2}(t) + S^{pop}_{W2P1}(t))}. \qquad (61)$$

For Supplementary Figure 2a, we sorted S^{pop}_{WxPy} data in population-specific matrices (rows with fixed Wx, columns with fixed Py) but did not normalize data to W1P1 condition or apply smoothing. We used these raw maps to test the symmetry in results, i.e., the difference in total spiking output with respect to the anti-diagonal (from lower left to upper right corner) within each population map. In Supplementary Figure 2b, we report raw spike output for every population, not sorted in matrices but in vectors: dashed lines, fixed Wx; solid lines, fixed Px.

Active pool dynamics. Active pool dynamics related to the change in fraction of active neurons per input K (Figure 3a) and the spiking activity in time for active neurons in the pool (Figure 3b). We got the average fraction of active neurons (Q) as

$$Q_{WxPy} = \frac{1}{K}\sum_{k=1}^{K}\frac{A}{N}, \qquad (62)$$

where A is the number of active neurons and N the population size. Identical to Figure 2a, we calculated ΔQ_{WxPy}, sorted the data in matrices and applied Gaussian smoothing to obtain the final heatmaps (Figure 3a).

In Supplementary Figure 3a, we provided population-specific differences between heatmaps from Figures 2a and 3a as $M'^{pop}_{Figure2a}/M'^{pop}_{Figure3a}$. Because Figure 2a showed mean number of spikes per conditions, while Figure 3a showed mean fraction of active neurons, their ratio revealed average number of spikes per average active neuron in each WxPy condition. We filtered these maps with a threshold where an average active neuron fires ≈1 spike (#Spikes/A > 1.1). These filtered maps were shown in Supplementary Figure 3b.

In Figure 3b, we reported mean spiking in time per active neuron as

$$S^{active}_{WxPy}(t) = \frac{1}{K}\sum_{k=1}^{K}\frac{y(t)}{A(t)}, \tag{63}$$

where, for every time bin t, we normalized the sum of spikes in that bin $y(t)$ with the number of active neurons in the bin $A(t)$, and then averaged over K inputs.

Input selectivity distributions and neuronal classification. As illustrated in Figure 4a, for every neuron i we found a fraction of inputs in which it spiked as

$$Y_i^{active} = \frac{1}{K}\sum_{k=1}^{K}(x_i > 0), \tag{64}$$

where $(x_i > 0)$ was 1 if the sum of spikes x_i for neuron i during input k was greater than 0, and 0 otherwise. We then sorted neurons into fraction bins (range: 0-1, bin size = 0.0025) to get population-specific distributions, which we normalized to the population size. We used these population-specific distributions to compute cumulative sums in Figure 4c, for six populations and four conditions (W1P1, W1P2, W2P1, W2P2).

In Figure 5a, we used the $(x_i > 0)$ threshold to classify neurons based on their responsiveness to input. For neuron i, if $(x_i > 0) = 1$ in all four conditions (W1P1, W1P2, W2P1, W2P2), it was labeled as input-invariant. If $x_i = 0$ in all conditions, it was labeled as silent. If $(x_i > 0) = 1$ in some, but $x_i = 0$ in other conditions, it was labeled as variant.

Presynaptic currents and E-I balance. In Figures 5 and 6, we reported presynaptic inputs $\sum_{syn} I_{syn}$ (Eq. (1)) for individual neurons across various WxPy conditions, and the ratio between excitatory-inhibitory (E-I) currents to address the E-I balance.

As illustrated in Supplementary Figure 5a, each neuron received inputs from four potential sources: recurrent excitatory (RCE; i.e. excitation from within its layer), recurrent inhibitory (RCI; i.e. inhibition from withing its layer), feedforward excitatory (FFE; i.e. excitation from the preceding layer) and feedforward inhibitory (FFI, i.e. inhibition from the preceding layer). Note that L4E, L4I and L3I lack FFI currents due to the connectivity architecture (Figure 1a).

For a postsynaptic neuron j, total presynaptic activity from RCE and FFE was captured in currents flowing through its postysnaptic AMPARs: $I^{RCE}_{AMPAR,j}$ and $I^{FFE}_{AMPAR,j}$, respectively (Eq. (52)). The total presynaptic RCI and FFI activity was captured in inhibitory currents flowing through its GABAaRs: $I^{RCI}_{GABAaR,j}$ and $I^{FFI}_{GABAaR,j}$, respectively (Eq. (53)). Although we were able to monitor four separate sources of presynaptic activity impinging on the postsynaptic neuron j, we did not have access to individual currents that made up each source. For instance, $I^{RCE}_{AMPAR,j}$ was a product of spiking activity from many presynaptic neurons within the same layer as the neuron j. We were able to ac-

cess identities of presynaptic neurons from connectivity matrices, but their individual impact on the postsynaptic neuron j was unavailable.

In Figure 5e,f, we showed the relationship between total excitatory and inhibitory drives for the neuron j. As illustrated in Figure 5c, to get total E drive, we summed RCE and FFE as

$$\sum I_j^{exc} = RCE_j + FFE_j, \tag{65}$$

where

$$RCE_j = \frac{1}{R} \sum_{rep=1}^{R} \sum_{k=1}^{K_{rep}} \int_{t_1^k}^{t_2^k} I_{AMPAR,j}^{RCE}(t)dt, \tag{66}$$

and

$$FFE_j = \frac{1}{R} \sum_{rep=1}^{R} \sum_{k=1}^{K} \int_{t_1^k}^{t_2^k} I_{AMPAR,j}^{FFE}(t)dt, \tag{67}$$

where R is the number of simulation repetitions for each WxPy condition (R=10), and K_{rep} is the number of detected thalamic events (i.e. inputs) in each repetition (K_rep ≈3.2), with $[t_1^k, t_2^k]$ being temporal boundaries for k-th input.

Similarly, to get the total I drive $\sum I_j^{inh}$, we summed RCI and FFI, where each current was obtained using the same approach as in Eqs. (66 and 67).

Finally, we used log($\sum I_j^{exc}$) (vertical axis, Figure 5e,f) and log($|\sum I_j^{inh}|$) (horizontal axis, Figure 5e,f) to illustrate E-I balance. In Supplementary Figure 4a,b, however, we used $EI_j =$ log($\sum I_j^{exc}/|\sum I_j^{inh}|$). We considered that the neuron j is in balance if $-0.5 < EI_j < 0.5$. We reported fraction of neurons with E-I balance for each population and the four conditions in Figure 5g,h.

Note that we reported relative RCE, RCI, FFE and FFI currents for the two neuronal classes, invariant and variant (see above for classification details), in Supplementary Figure 5 as

$$C^{class} = \frac{1}{N^{class}} \sum_{j}^{N^{class}} C_j, \tag{68}$$

where C stands for either current source (RCE, RCI, FFE, FFI) and N^{class} is the number of neurons in each class. In each class, we obtained relative current C_r by normalizing C as $C_r = C/(RCE + RCI + FFE + FFI)$ independent for each population. Relative currents per population and across the four WxPy coditions were shown in Supplementary Figure 5c for invariant neurons and Supplementary Figure 5d for variant. We showed their population-specific differences within condition in Supplementary Figure 5b.

In Figure 6, we included all simulated WxPy conditions into the analysis. We averaged excitatory and inhibitory currents from neurons in each class (invariant and variant) as

$$E^{class}_{WxPy} = \frac{1}{N^{class}} \sum_{j}^{N^{class}} \sum I^{exc}_{WxPy,j} \tag{69}$$

and

$$I^{class}_{WxPy} = \frac{1}{N^{class}} \sum_{j}^{N^{class}} \sum I^{inh}_{WxPy,j}, \tag{70}$$

where N^{class} is the number of neurons in each class. We showed E^{class}_{WxPy} and I^{class}_{WxPy} for invariant neurons in orange and pink, respectively, in Figure 6c for all WxPy conditions. Similarly, we showed E^{class}_{WxPy} and I^{class}_{WxPy} for variant neurons in black and blue, respectively, in Figure 6c.

To get the E-I balance scores for each class across all conditions, we computed their ratios as $E^{class}_{WxPy}/I^{class}_{WxPy}$, shown in Figure 6a for invariant and Figure 6b for variant neurons. In Supplementary Figure 6b, we showed the relative difference in excitatory drive between invariant and variant neurons as

$$\Delta E = \frac{E^{invariant} - E^{variant}}{E^{variant}}, \tag{71}$$

and in Supplementary Figure 6c, we did the same for the relative difference in inhibitory drive between classes.

Supplementary data and figures

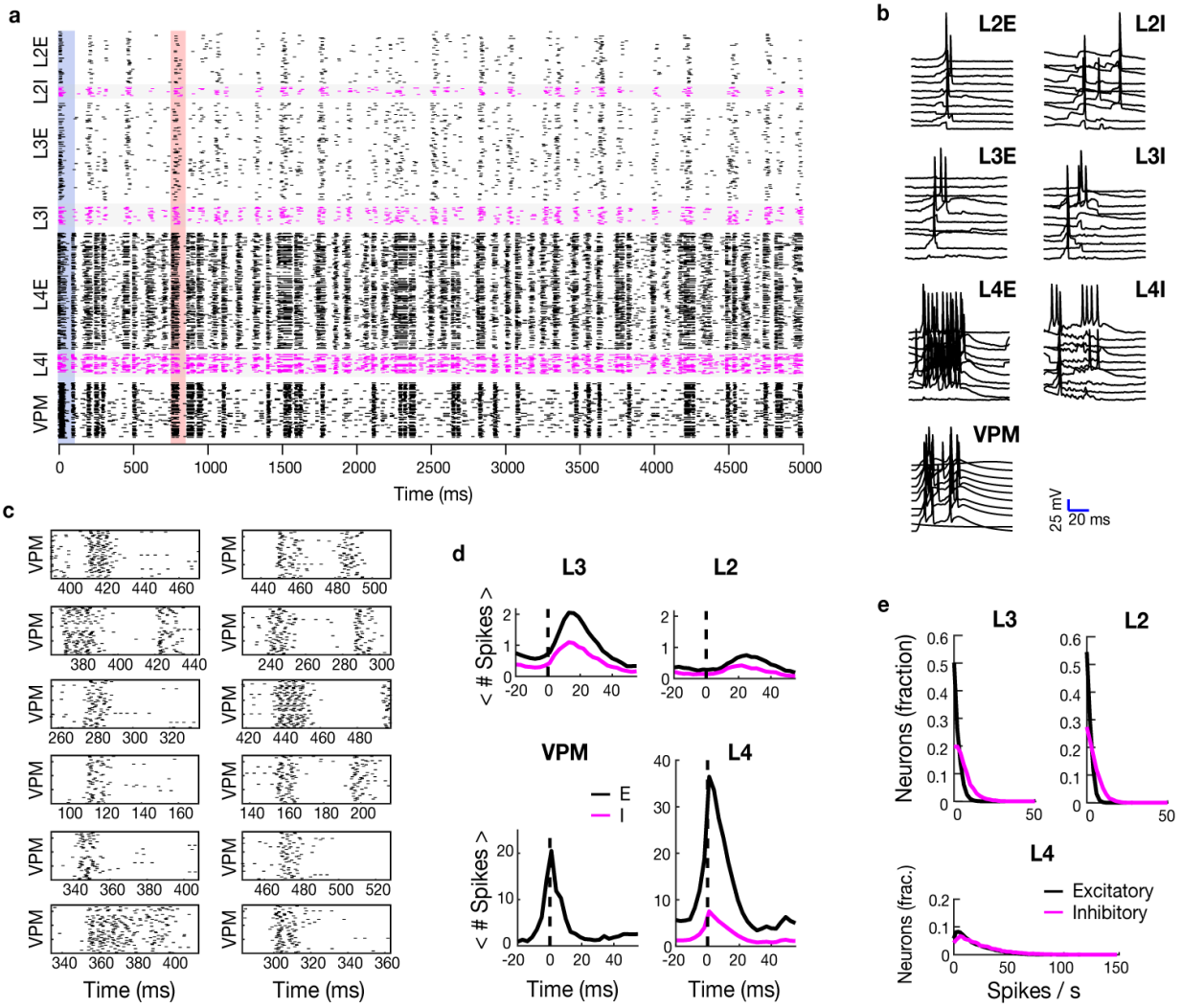

Supplementary Figure 1: Raw activity in multi-layered spiking neural network (mlSNN) with baseline quantification.

(**a**) Raster plot for one network realization with initial connectivity parameters (W1P1; Online Methods). Vertical axis, neurons from six cortical populations (from bottom to top: L4I, L4E, L3I, L3E, L2I, L2E, and thalamic population: VPM). Pink dots, spikes from inhibitory neurons. Black dots, spikes from excitatory neurons. The gray background behind inhibitory spikes is for better contrast. Horizontal axis, time in ms. Activity is triggered by a Poissonian process (not shown) coupled with thalamic neurons. Blue shade, 0-100 ms of discarded activity due to network settling effects. Red shade, the boundary for one detected thalamic input pattern (bottom raster) spiking shown in **b**.

(**b**) Example membrane potential of 10 randomly selected neurons from the thalamic population (VPM) and six cortical populations (see titles). Activity corresponds to the red shade from simulation in **a**.

(**c**) Raster plots (N = 12) of thalamic activity which qualified as input patterns (Online Methods). The activity was taken from random network realisations (N = 4) with different W-P parameters.

(**d**) Peristimulus time histograms (bin length = 3 ms, time in the horizontal axis) per layer showing the mean number (#) of spikes (vertical axis) for excitatory (black) and inhibitory (pink) populations averaged across multiple input patterns (N=71; 20 simulations, 600 ms each). Dashed line, peak activity in the thalamus (VPM).

(**e**) Firing rate (Spikes / s, horizontal axis) distributions (PDF, neuron fraction; vertical axis) for excitatory (black) and inhibitory (pink) populations sorted in layers (see titles). Spikes were counted from full simulation time, excluding the 0-100ms considered as the network settling window. Data averaged across 400 simulations (600 ms each).

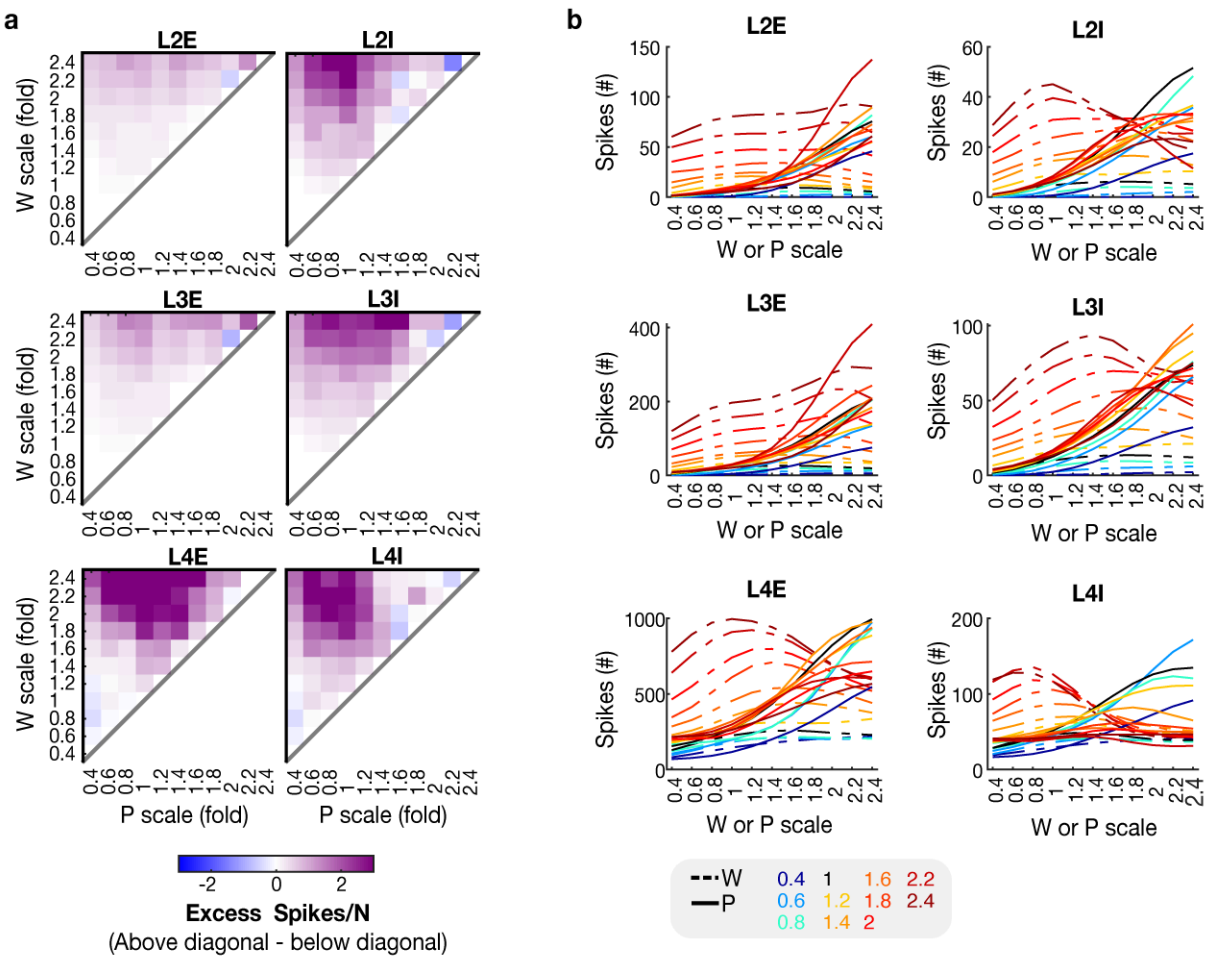

Supplementary Figure 2: The effects of metaplasticity on activity in mlSNN.

(**a**) Subtraction of evoked number of spikes per neuron (N) after network-wide in scaling synaptic weights (W, vertical axis) and connectivity probability (P, horizontal) in conditions below the anti-diagonal (in grey) from conditions above. Colour code: difference evoked spikes / N. Population labels in titles above heatmaps.

(**b**) Raw spike number (#) per population (see titles) after network-wide scaling in synaptic weights (W, vertical axis) and connectivity probability (P, horizontal). Dashed lines, W scale in colour (see legend), with P scale on the horizontal axis. Solid lines, P scale in colour with W scale on the horizontal axis.

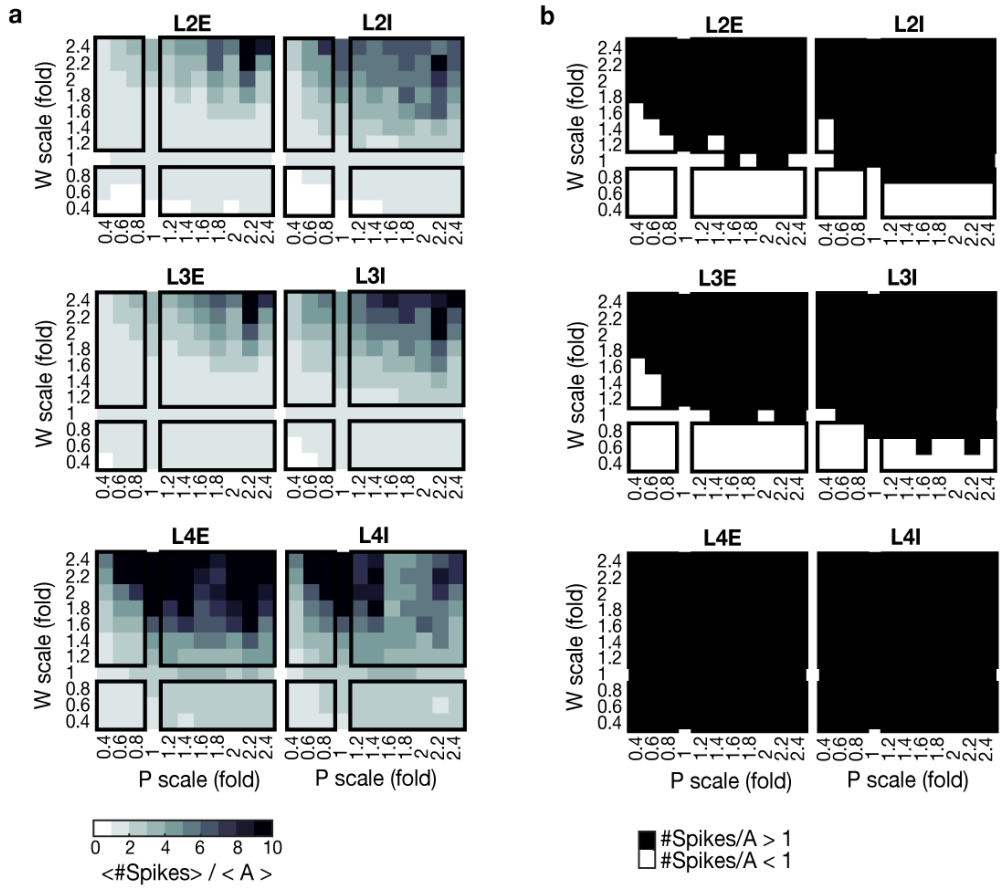

Supplementary Figure 3: Change in the spiking output per active neuron after W-P scaling.

(**a**) Division of the number of spikes per W-P condition (Figure 2a) by the active neurons per condition (Figure 3a). Vertical axis, W scaling. Horizontal axis, P scaling. Colour scale: Spikes per active (A) neuron. Population names in titles.

(**b**) Population (see titles) masks are created by filtering maps from **a** using a threshold: greater than 1 spike/A (black) or less than 1 spike/A (white).

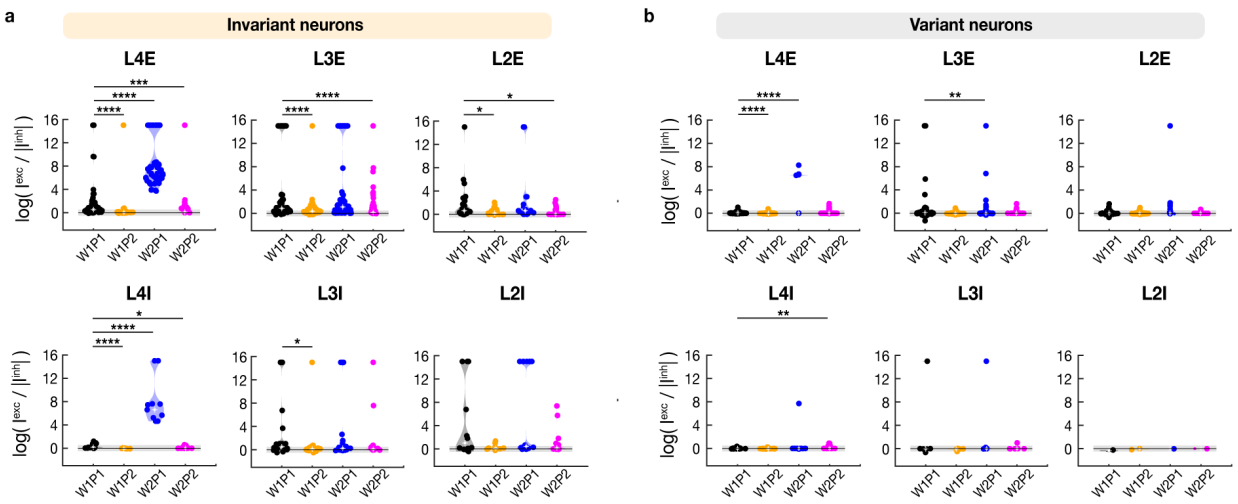

Supplementary Figure 4: Statistical comparisons between presynaptic current-driven states in distinct neuronal subtypes.

(**a**) Six population-related (in titles) panels representing the log-transformed ratio of excitatory to inhibitory presynaptic currents ($\log(I^{exc} / |I^{inh}|)$ in individual neurons (dots) from input-invariant subtype (see Figure 5b) under four plasticity conditions: black, W1P1; orange, W1P2; blue, W2P1; pink, W2P2. Statistical significance between W1P1 and other conditions based on the Wilcoxon signed-rank test with Bonferroni correction (*, $p<0.05$; **, $p<0.01$; ***, $p<0.005$; ****, $p<0.001$). For visualisation purposes, log-values >15 were constrained to 15.

(**b**) Same but for variant neurons from Figure 5b.

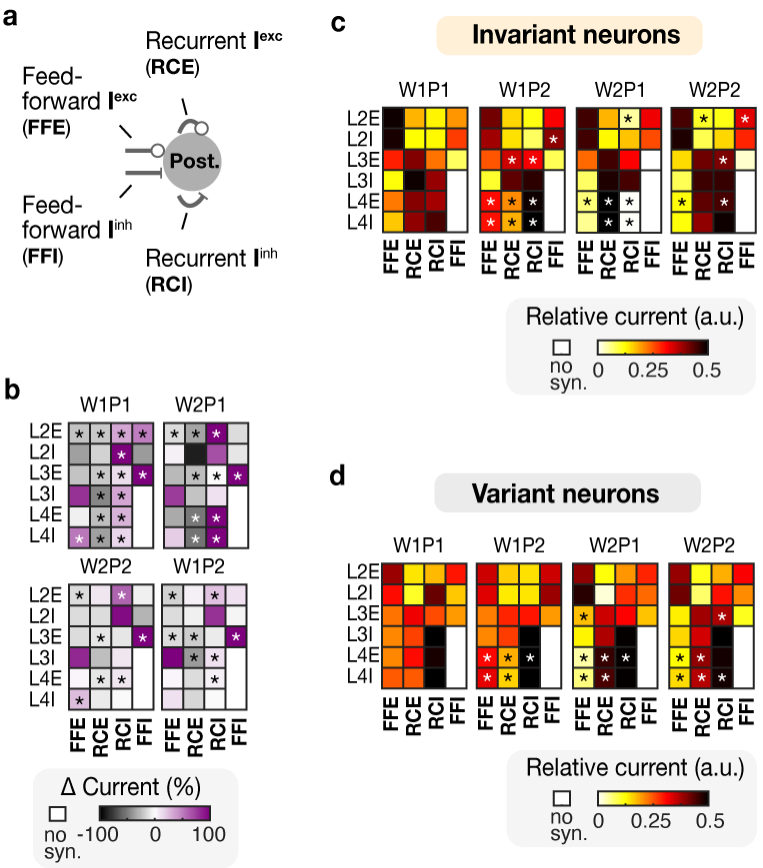

Supplementary Figure 5: Differences in presynaptic currents explain states of neuronal subtypes pre- and post-(meta)plasticity.

(**a**) Illustration of the analysis behind data in **b**-**d**: currents from Figure 5c are dissected in subtypes — recurrent (coming from the same layer) and feedforward (coming from the preceding layer).

(**b**) Differences in relative current subtypes (horizontal axis: FFE, feedforward excitation; RCE, recurrent excitation; RCI, recurrent inhibition; FFI, feedforward inhibition) between input-invariant and variant neurons (Figure 5b) across six populations (vertical axis) and four conditions (in titles: (top left) W1-P1, (top right) W2-P1, (bottom left) W2-P2 and (bottom right) W1-P2. Color scale (below) applies to all maps. Significance is based on the Wilcoxon signed-rank test with Bonferroni correction (*, $p<0.05$).

(**c**) For invariant neurons (orange fractions from Figure 5b), the relative contribution of the four presynaptic currents (horizontal axis) in every population (vertical axis). Heatmaps are ordered per condition (in titles): (1) W1-P1, (2) W1-P2, (3) W2-P1 and (4) W2-P2. Relative current contribution shown in colorbar below heatmaps. Current subtypes shown in **a**: FFE,

feedforward excitation; RCE, recurrent excitation; RCI, recurrent inhibition; FFI, feedforward inhibition. L4E, L4I and L3I do not have FFI (in colorbar: no syn., no synapse). Asterisks in squares show significant differences between matched current types from any condition compared to W1P1. Significance is based on the Wilcoxon signed-rank test with Bonferroni correction (*, $p<0.05$).

(**d**) Same as in **c** but for variant neurons (grey fractions from Figure 5b).

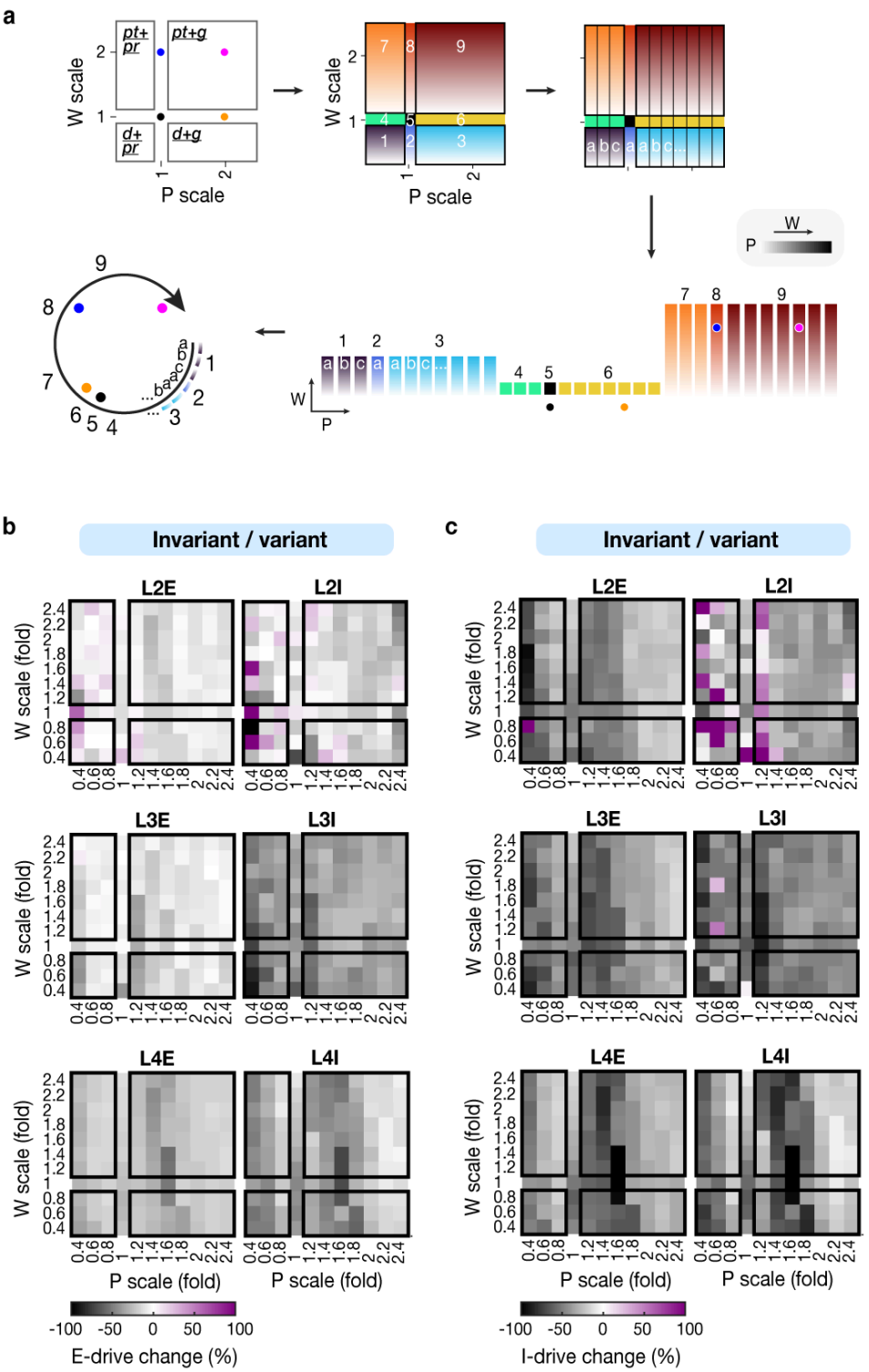

Supplementary Figure 6: Relative differences in excitatory and inhibitory currents between distinct neuronal subtypes.

(**a**) Illustration of the data organisation in Figure 6c: the 2D (meta)plasticity plane (first cartoon) used in Figures 2 and 3 was mapped in 9 fields (second cartoon, numbered labels).

Fields correspond to quadrants (metaplasticity) and between-quadrants (plasticity) conditions. Color codes are random. The 2D map with fields was vertically parcellated (third cartoon, alphabetic labels) into subgroups of conditions (fourth cartoon, bars with alphabetic labels). Bars represent a fixed P and increasing W if filled with a gradient (see legend on top). Solid-color bars (fields 4-6) have fixed P and W. The dots below or on some bars are from the four networks (first cartoon) in analysed in detail throughout the paper. Subgroups of conditions were arranged in a circle in the clockwise direction, starting from the quadrant with the lowest number (see second cartoon). The dots show where their conditions would appear on the circle.

(**b**) Relative change (%) in the mean excitatory current drive between input-invariant and variant neurons across W-P conditions from Figure 6c (black vs orange). Vertical axis, W scaling. Horizontal axis, P scaling. Color scale, below L4E applies to all maps. Population names in titles.

(**c**) Same as in **b** but for the mean inhibitory current drive (blue vs pink, Figure 6c)

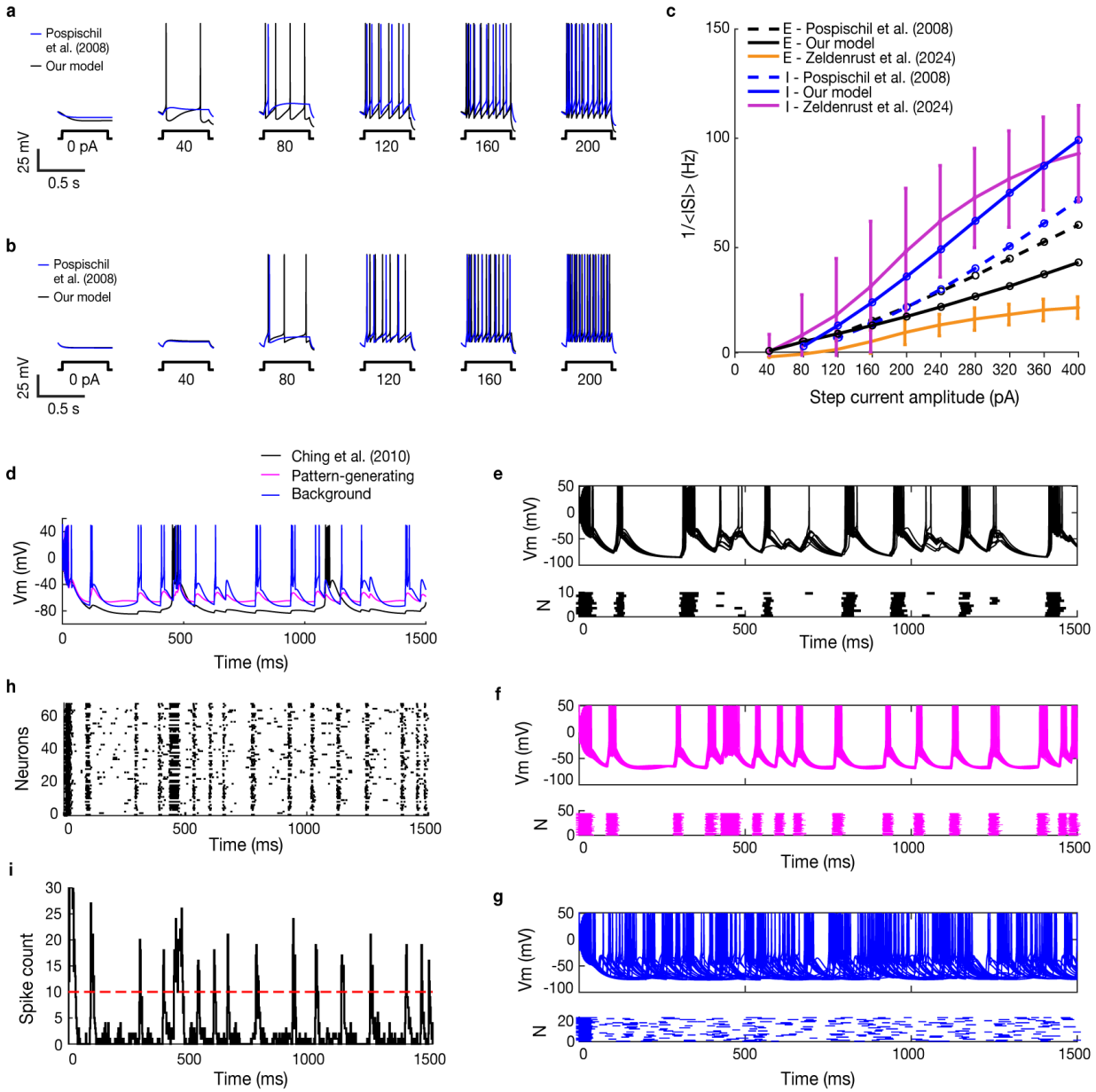

Supplementary Figure 7: Input-output fitting procedures for cortical and thalamic neuron models.

(**a**) Fitting of the Hodgkin-Huxley model representing excitatory neuron dynamics with a step-current protocol. Current pulses with amplitudes (below each step) were injected directly into the model for 500 ms. We used the default model from Pospischil et al. (2008) (blue) and adjusted the parameters (Methods) to match neurons from Zeldenrust et al. (2024) (black, our model).

(**b**) Same as in **a** but for inhibitory neurons.

(**c**) Excitatory and inhibitory neurons in three stages: default values from Pospischil et al. (2008), desired dynamics from Zeldenrust et al. (2024), fitted dynamics used in our model. See labels for color codes. Vertical axis, firing rate calculated as an inverse of the mean inter-spike interval (ISI) at every current amplitude (horizontal axis).

(**d**) Fitting of the Hodgkin-Huxley model representing thalamocortical relay (TCR) dynamics. Fitting was performed without an explicit protocol, by manually adjusting the parameters (Methods) to shift the default neuron (black) from Ching et al. (2010) to depolarized states. In pink, neuron dynamics used to generate inputs (Methods); in blue, neuron dynamics used to generate background noise (Methods).

(**e**) Population-level spiking from a default TCR neuron from **d**. Vertical axis, membrane potential; horizontal axis, time.

(**f**) Population-level spiking from a fitted, input-generating TCR neuron from **d** used in our model. Vertical axis, membrane potential; horizontal axis, time.

(**g**) Population-level spiking from a fitted, background-generating TCR neuron from **d** used in our model. Vertical axis, membrane potential; horizontal axis, time.

(**h**) Spiking from **f** and **g** combined in a raster plot. Vertical axis, neurons; horizontal axis, time. Black dots, spikes.

(**i**) Peristimulus time histogram from data in **h**. Vertical axis, spike cound; horizontal axis, time. Red line, the the approximate threshold for detecting peaks in thalamic activity (Methods).

Supplementary Table 1: Parameter values for sodium (Na), delayed-rectifier potassium (KDR), slow non-inactivating potassium (M) and leak (L) channels used to model cortical E and I neurons. Values in brackets are default values from (Pospischil et al., 2008) which we changed to the outside-bracket values to adjust the neuron frequency-current behaviour (see the text).

Parameter	E values	I values
g_{Na}	0.086 (0.056) S/cm^2	0.078 (0.058) S/cm^2
E_{Na}	50 mV	50 mV
g_{KDR}	0.006 S/cm^2	0.0039 S/cm^2
E_{KDR}	-90 mV	-90 mV
g_M	18 (7.5) $\times$ 10^5 S/cm^2	5 (7.87) $\times$ 10^5 S/cm^2
τ_{max}	808 (608) ms	602 (502) ms
g_{leak}	0.85 (2.05) $\times$ 10^5 S/cm^2	3.8 $\times$ 10^5 S/cm^2
E_{leak}	-69 (-70.3) mV	-70.4 mV
V_T	-64 (-56.2) mV	-58 (-57.9) mV

Supplementary Table 2: Parameter values used for simulating VPM neurons, and for their activation with a Poisson-based input.

Parameter	Equation	Ching *et al.* (2010)	Pattern-generating	Background
g_h	38	0.001 mS/cm^2	0.01 mS/cm^2	0.005 mS/cm^2
N	49	10	45	24
g_{In}	49	0.05 mS/cm^2	0.5 mS/cm^2	0.75 mS/cm^2
r	-	12 Hz	9 Hz	5 Hz
P_{In}	-	0.5	0.3	0.1
α	50	10	14	25
τ_r	50	0.5 ms	0.5 ms	0.5 ms
τ_d	50	2 ms	2 ms	2 ms

Supplementary Table 3: Parameter values for excitatory (glutamatergic) and inhibitory (GABAergic) conductance-based synapses. g_{AMPA} was defined twice: the value outside brackets is for cortico-cortical synapses, the value inside brackets is for thalamocortical synapses.

Parameter	AMPAR	GABAaR
g_{syn}	0.017 (0.034) mS/cm^2	0.125 mS/cm^2
E_{syn}	0 mV	-80 mV
τ_{rise}	0.4 ms	0.2 ms
τ_{decay}	2 ms	10 ms

Supplementary Table 4: Number of neurons across the network. L, layer; E, excitatory; I, inhibitory.

Neuron type/Layer	L4	L3	L2	VPM
E	188	158	86	69
I	33	28	15	-

Supplementary Table 5: Synapse-specific weights (W) and connection probabilities (P) used in the model.

Pre-post population	Pre-post neuron type	W	P
L2 →L2,	E-E	2.8	5.6%
L3 →L2	E-I	8.1	5.1%
and	I-E	17	5.9%
L3 →L3	I-I	15	5.1%
	E-E	2.4	5.8%
L4 →L3	E-I	5.7	0.33%
	I-E	14	1.7%
	E-E	3.3	7.6%
L4→L4	E-I	7.9	4.2%
	I-E	16	6.3%
	I-I	14	6.2%
VPM →L4	E-E	2.45, 4.55	1.5%, 2.79%
	E-I	3.15, 5.85	1.75%, 3.25%

Supplementary Table 6. Quantification of the spiking activity from Figure 2a. First two columns: outside brackets, maximum (Max, 1st column) and minimum (Min, 2nd column) amplitude of relative change (Δ%) in spikes per neuron (N, within brackets) across each population-related heatmap in Figure 2a. Also within brackets, W-P conditions at which Max and Min were evoked (x for W scale, y for P scale. From 3rd to 6th column, for W-P condition (outside brackets), reporting detected spikes per neuron (within brackets, mean ± standard deviation). Population names (across rows), pertain to data one row below.

Max Δ% (Spikes/N @ WxPy)	**Min Δ% (Spikes/N @ WxPy)**	**W1P1 (Spikes/N)**	**W2P1 (Spikes/N)**	**W2P2 (Spikes/N)**	**W1P2 (Spikes/N)**
L2E					
1658.68% (1.72±0.65 @ W2.4-P2.2) ****	**-100% (0±0 @ W0.4-P0.4) ******	0.1±0.1	**0.58±0.44 ******	**0.4±0.27 ******	0.11±0.12
L2I					
832.8% (3.77±2.15 @ W2.4-P0.8) ****	**-100% (0±0 @ W0.4-P0.4) ******	0.4±0.37	**2.54±1.41 ******	**2.31±1.13 ******	0.34±0.29
L3E					
1636.84% (2.79±0.9 @ W2.4-P2.2) ****	**-100% (0±0 @ W0.4-P0.4) ******	0.16±0.13	**0.9±0.58 ******	**0.81±0.47 ******	0.13±0.09
L3I					
918.02% (4.04±1.25 @ W2.4-P1.6) ****	**-100% (0±0 @ W0.4-P0.4) ******	0.4±0.26	**2.05±0.95 ******	**2.41±1.05 ******	0.43±0.28
L4E					
364.39% (5.87±1.04 @ W2.4-P0.6) ****	**-73.36% (0.34±0.18 @ W0.4-P0.4) ******	1.26±0.69	**4.31±1.42 ******	**3.31±1.29 ******	1.08±0.42
L4I					
300.6% (5.55±1.79 @ W2.2-P0.6) ****	**-66.83% (0.46±0.25 @ W0.6-P0.4) ******	1.39±0.57	**3.76±1.23 ******	1.48±0.96	**1.04±0.39 ***

Supplementary Table 7. Quantification of the fraction of active neurons (A/N) from Figure 3a. First two columns: outside brackets, maximum (Max, 1st column) and minimum (Min, 2nd column) amplitude of relative change (Δ%) in fraction (within brackets) across each population-related heatmap in Figure 3a. Also within brackets, W-P conditions at which Max and Min were evoked (x for W scale, y for P scale. From 3rd to 6th column, for W-P condition (outside brackets), reporting detected fractions (within brackets, mean ± standard deviation). Population names (across rows), pertain to data one row below.

Max Δ% (A/N @ WxPy)	**Min Δ% (A/N @ WxPy)**	**W1P1 (A/N)**	**W2 (A/N)**	**W2P2 (A/N)**	**P2 (A/N)**
L2E					
244.76% (0.32±0.21 @ W2.2-P0.4) ***	**-100% (0±0 @ W0.4-P0.4) ******	0.09±0.09	**0.22±0.1 *****	0.12±0.05	0.09±0.1
L2I					
117.87% (0.59±0.13 @ W2.4-P0.6) ****	**-100% (0±0 @ W0.4-P0.4) ******	0.27±0.21	**0.49±0.17 ****	**0.39±0.1 ***	0.21±0.12
L3E					
173.22% (0.4±0.13 @ W2.4-P0.8) ****	**-100% (0±0 @ W0.4-P0.4) ******	0.15±0.11	**0.34±0.13 ******	**0.24±0.07 ****	0.12±0.08
L3I					
109.09% (0.59±0.11 @ W2.2-P1) ****	**-100% (0±0 @ W0.4-P0.4) ******	0.28±0.14	**0.52±0.17 ******	**0.41±0.11 *****	0.28±0.14
L4E					
29.69% (0.6±0.23 @ W2.2-P0.4) ***	**-48.74% (0.24±0.02 @ W2.2-P2.2) ******	0.47±0.11	**0.38±0.03 *****	**0.33±0.09 ******	0.43±0.13
L4I					
30.41% (0.64±0.23 @ W1.6-P0.4) ***	**-78.8% (0.1±0.02 @ W2.2-P2.2) ******	0.49±0.14	**0.33±0.03 ******	**0.25±0.16 ******	0.48±0.15